SFN Letters速報ゼミ

July 15, 2021

古屋 玲

#342 24-28担当

24. **Thermal Wave Instability as an Origin of Gap and Ring Structures in Protoplanetary Disks**
Takahiro Ueda, Mario Flock, Tilman Birnstiel ★ Recent millimeter and infrared observations have shown that gap and

20

25. **Multicolor Variability of Young Stars in the Lagoon Nebula: Driving Causes and Intrinsic Timescales**
Laura Venuti, Ann Marie Cody, Luisa M. Rebull, Giacomo Beccari, Mike Irwin, Sowmya Thanvantri, Steve B. Howell, Geert Barentsen ★ Space observatories have provided unprecedented depictions of the many variability behaviors

09 から 15：やや質量の大きい若い星の時間変動観測, 解析は緻密, 星と円盤がcorotationする半径の質量依存性を明らかにした.

26. **Tree-based solvers for adaptive mesh refinement code FLASH – II: radiation transport module TreeRay**
Richard Wünsch, Stefanie Walch, František Dinnbier, Daniel Seifried, Sebastian Haid, Andre Klepitko, Anthony P. Whitworth, Jan Palouš ★ The treatment of radiative transfer with multiple radiation sources is a critical challenge in

16 から 19：現実的なシュミレーションのために輻射場の取り扱い法を研究：輻射の源が複数の場合かつ広いエネルギー域の計算を可能にした.

27. **No impact of core-scale magnetic field, turbulence, or velocity gradient on sizes of protostellar disks in Orion A**
Hsi-Wei Yen, Bo Zhao, Patrick M. Koch, Aashish Gupta ★ We compared the sizes and fluxes of a sample of protostellar

05 から 08：研究目標はこの分野の最重要課題. 物理的因果関係がないから無相関だったのかもしれないが, 解析の粗さが目立つ, それに起因?

28. **TIMES I: a Systematic Observation in Multiple Molecular Lines Toward the Orion A and Ophiuchus Clouds**
Hyeong-Sik Yun, Jeong-Eun Lee, Yunhee Choi, Neal J. Evans II, Stella S. R. Offner, Mark H. Heyer, Brandt A. L. Gaches, Yong-Hee Lee, Giseon Baek, Minho Choi, Hyunwoo Kang, Seokho Lee, Ken'ichi Tatematsu, Yao-Lun Yang, How-Huan Chen, Youngung Lee, Jae Hoon Jung, Changhoon Lee, Jungyeon Cho ★ We have

01 から 04：オリオン南部を含めたおそらく始めての多輝線観測. 基本的なデータの提示論文.
だが堅実な解析, 続編を大いに期待.

28. TIMES I: a Systematic Observation in Multiple Molecular Lines Toward the Orion A and Ophiuchus Clouds

Hyeong-Sik Yun, Jeong-Eun Lee, Yunhee Choi, Neal J. Evans II, Stella S. R. Offner, Mark H. Heyer, Brandt A. L. Gaches, Yong-Hee Lee, Giseon Baek, Minho Choi, Hyunwoo Kang, Seokho Lee, Ken'ichi Tatematsu, Yao-Lun Yang, How-Huan Chen, Youngung Lee, Jae Hoon Jung, Changhoon Lee, Jungyeon Cho ★ We have

ABSTRACT

We have used the Taeduk Radio Astronomy Observatory to observe the Orion A and Ophiuchus clouds in the J =1−0 lines of ^{13}CO, C^{18}O, HCN, HCO$^+$, and N_2H^+ and the J =2−1 line of CS. The fully sampled maps with uniform noise levels are used to create moment maps. The variations of the line intensity and velocity dispersion with total column density, derived from dust emission maps, are presented and compared to previous work. The CS line traces dust column density over more than one order of magnitude, and the N_2H^+ line best traces the highest column density regime ($\log(N_{H_2}) > 22.8$). Line luminosities, integrated over the cloud, are compared to those seen in other galaxies. The HCO$^+$-to-HCN luminosity ratio in the Orion A cloud is similar to that of starburst galaxies, while that in the Ophiuchus cloud is in between those of active galactic nuclei and starburst galaxies.

2.1. *The TRAO 13.7 m Telescope*

We obtained six molecular line maps toward each cloud using the 13.7-m radio telescope at TRAO in Daejeon, South Korea. The SEQUOIA-TRAO receiver, which has 16-pixels arranged in a 4×4

resolution is about 15 kHz, corresponding to a velocity resolution of about 0.04 km s^{-1} at 110 GHz. The main beam of the TRAO telescope has an almost circular pattern with a beam size of about 57″

During the observation, the pointing uncertainty is less than 10″. The system noise temperature

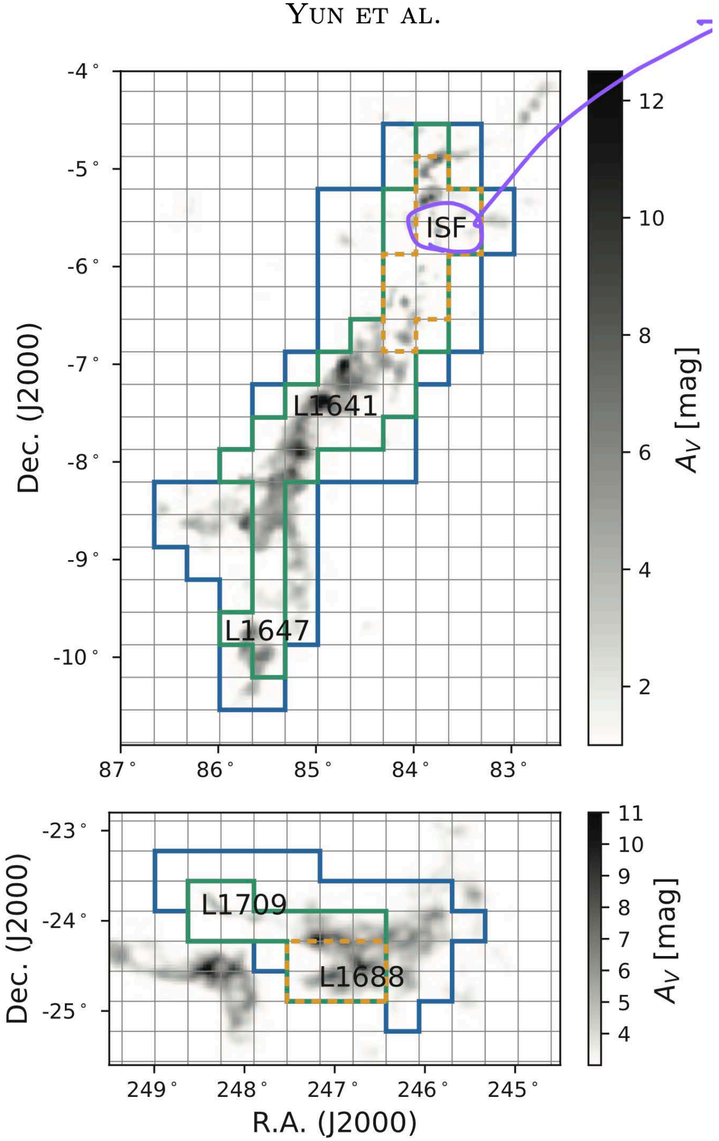

Figure 1. Visual extinction map of the Orion A (top) and Ophiuchus (bottom) clouds provided by Dobashi et al. (2005) overlaid with outlines showing 20′ × 20′ submaps (the gray vertical and horizontal lines). The mapped area in ^{13}CO J=1−0, C^{18}O J=1−0, HCN J=1−0, and HCO$^+$ J=1−0 is presented in the blue solid line. The green solid line shows the area where N_2H^+ J=1−0 and CS J=2−1 are mapped. For the active star-forming regions, such as ISF, L1641-N cluster (in the Orion A cloud) and L1688 (in the Ophiuchus cloud) that outlined with the orange dotted lines, the N_2H^+ and CS lines are mapped more deeply.

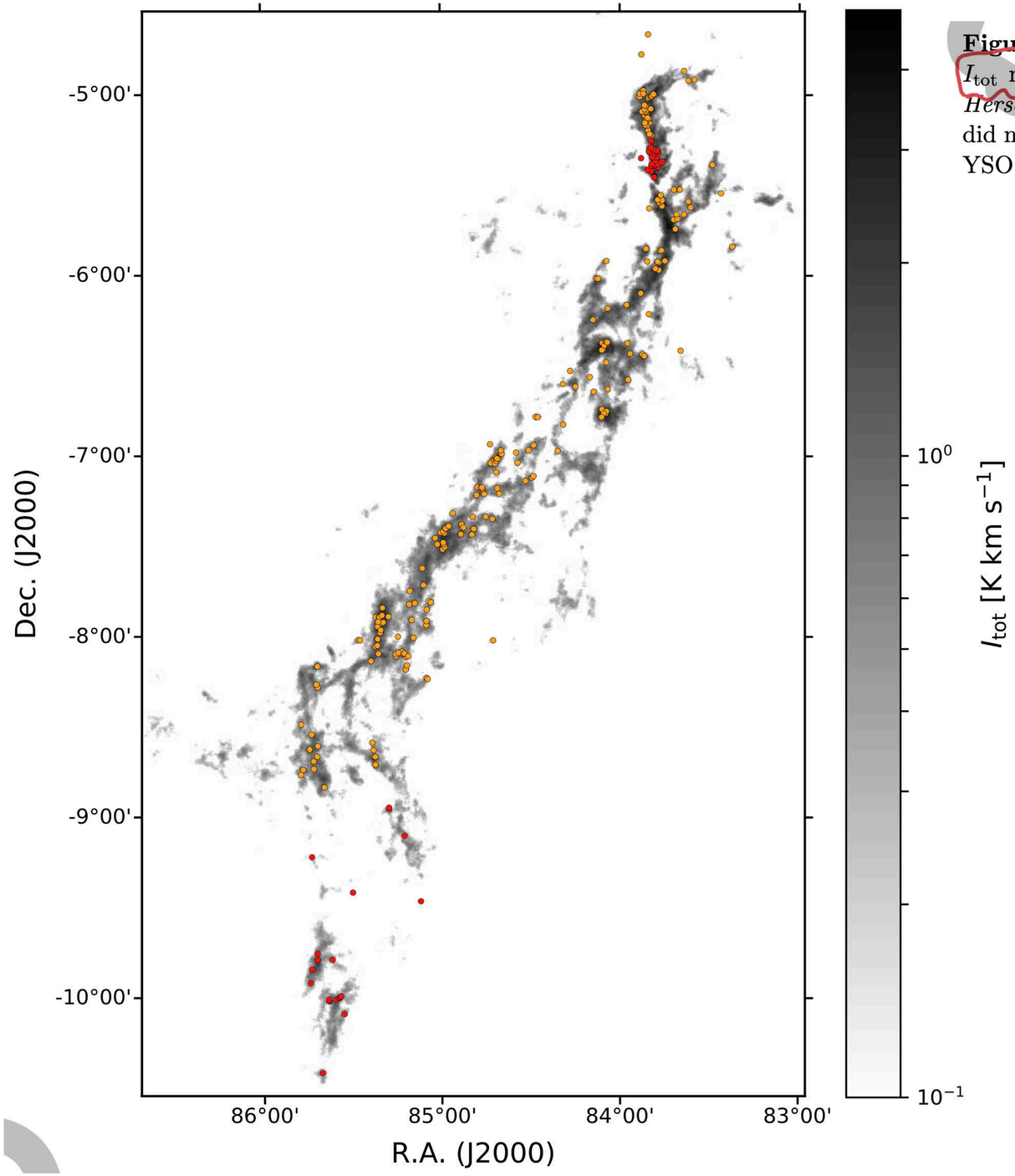

Figure 9. Distribution of young embedded protostars in the Orion A cloud. The background image is the $I_{\rm tot}$ map of $C^{18}O$. The Class 0/I young stellar objects (YSOs) and flat spectrum sources, identified with *Herschel* space observatory (Furlan et al. 2016), is presented in orange circles. Since Furlan et al. (2016) did not provide YSOs near the Orion Nebula and the southernmost part of the cloud, we adopt the *Spitzer* YSO catalog provided by Megeath et al. (2012) (red circles).

Figure 13. Distribution of young embedded protostars in the Ophiuchus cloud. The background image is the $I_{\rm tot}$ map of $C^{18}O$, and the YSO catalog provided by Dunham et al. (2015) is presented in red circles.

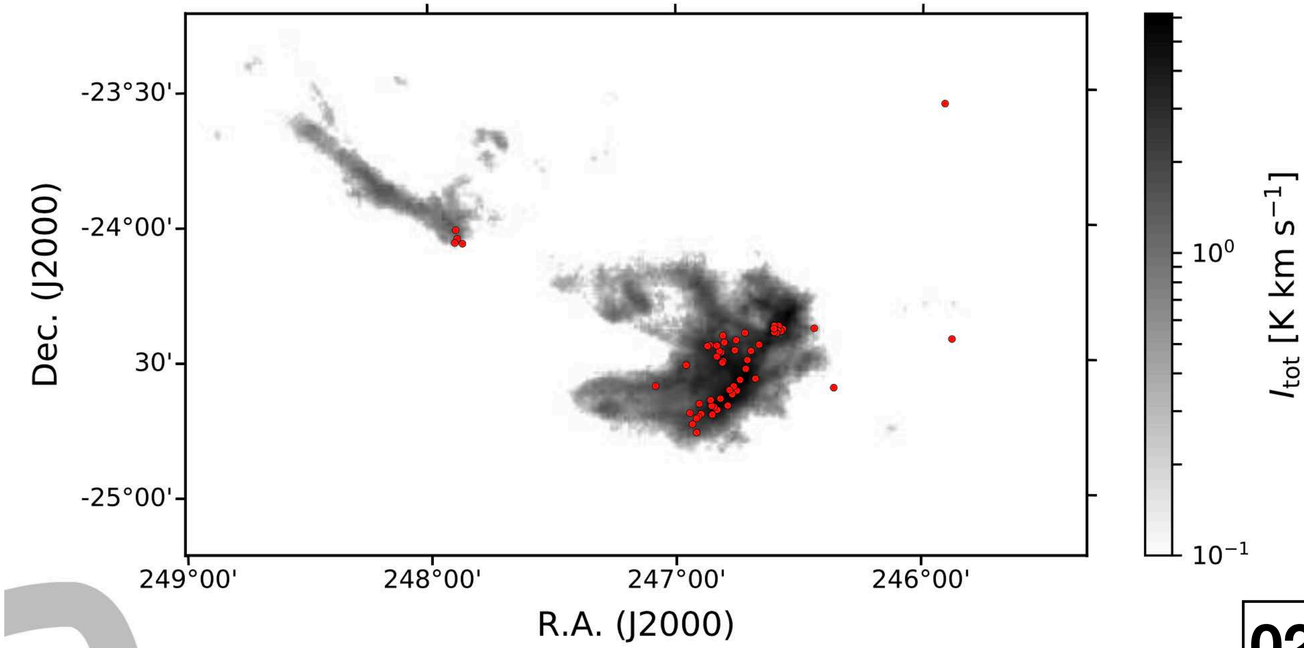

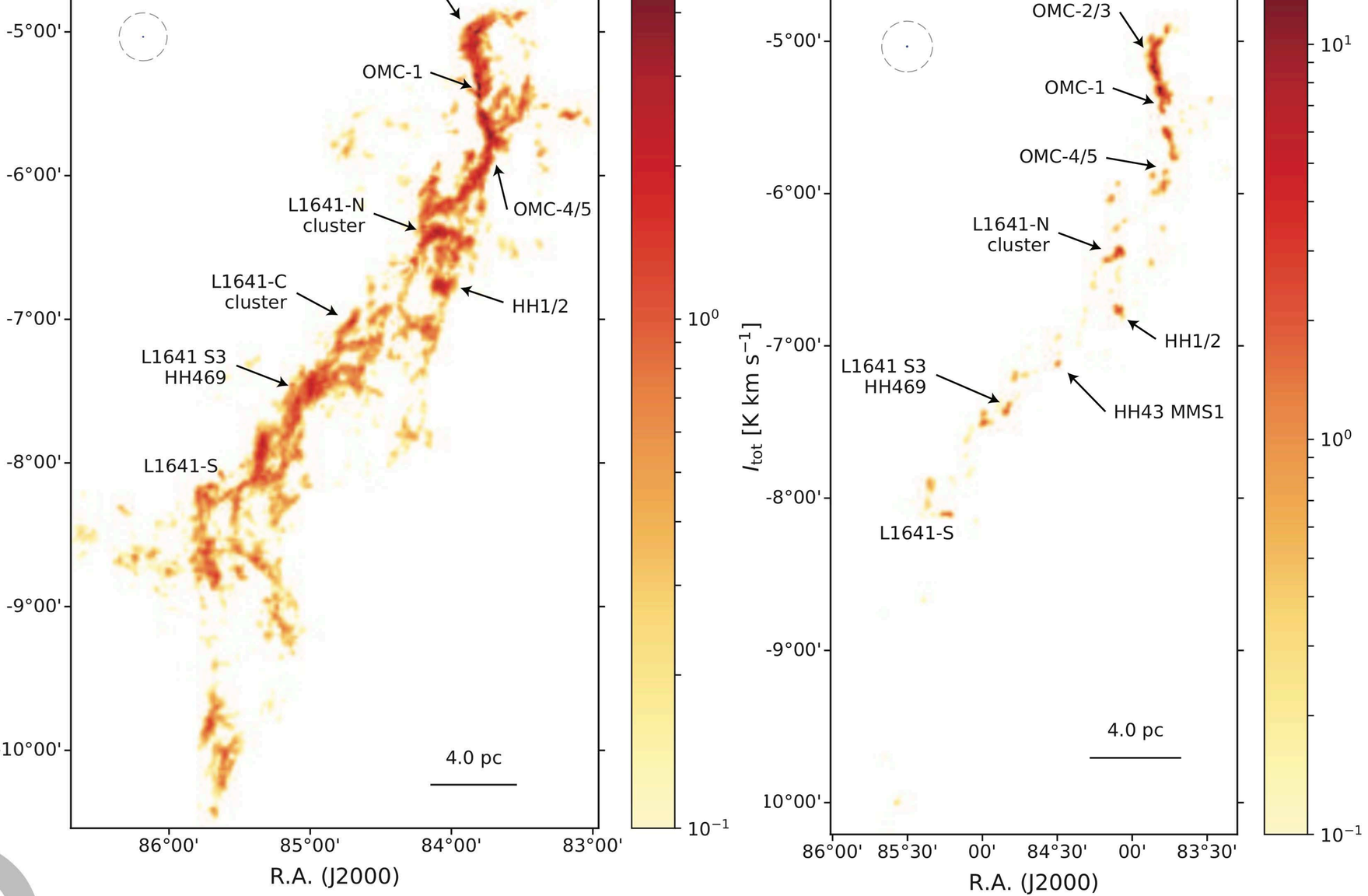

The same as Figure 2 but for the $C^{18}O$ line. We annotated the $C^{18}O$ map with the n
d sources (Davis et al. 2009; Meingast et al. 2016; Mairs et al. 2016).

We derived N_{H_2} from the observations of dust continuum emission that can trace the amount of gas in a cloud (Goodman et al. 2009). The N_{H_2} maps were derived by fitting a modified blackbody (MBB) into the spectral energy distribution (SED) of the continuum emission from cold dust. Archival *Herschel* PACS (160 μm) and SPIRE (250, 350, and 500 μm) continuum observations that were obtained as part of the *Herschel* Gould Belt Survey (André et al. 2010) are adopted. Note that

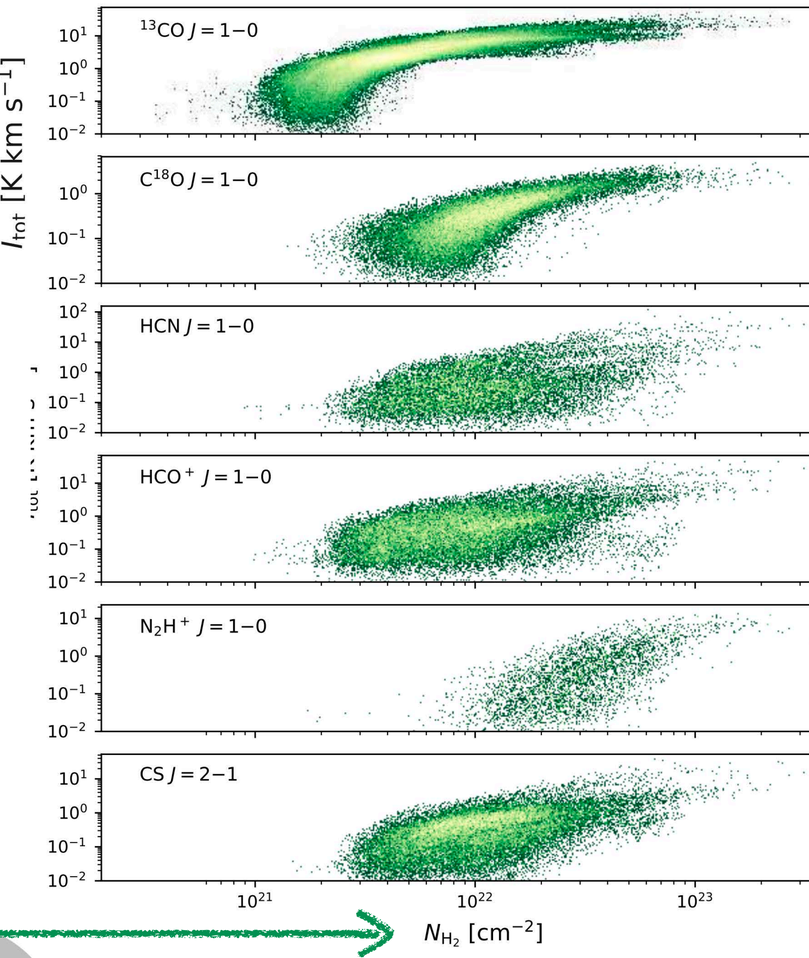

Figure 15. Comparison of I_{tot} and column density (N_{H_2}) in the Orion A cloud. From the panels, the diagrams show for the ^{13}CO, $C^{18}O$, HCN, HCO^+, N_2H^+, and CS lines.

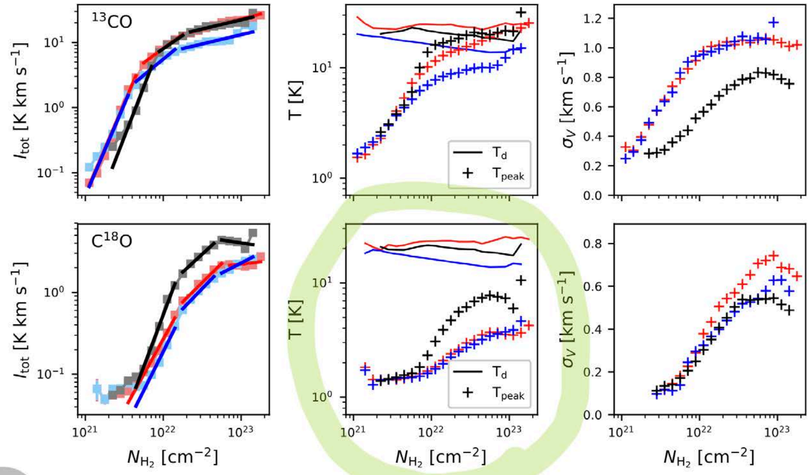

Figure 17. Variation of means of I_{tot} (left), T_{peak} (middle), and σ_V (right) for the ^{13}CO (top) and C^{18}O (bottom) lines. The red, blue, and black colors indicates the results for the ISF, L1641, and Ophiuchus regions. The mean I_{tot} values and their 1-σ error ranges are presented in square symbols and errorbars with weak colors. The red, blue, black solid lines indicates the power-law fitting results. In the middle panel, the mean T_{peak} values are presented in the plus symbols, and the variations of mean T_d values are also exhibited in solid lines.

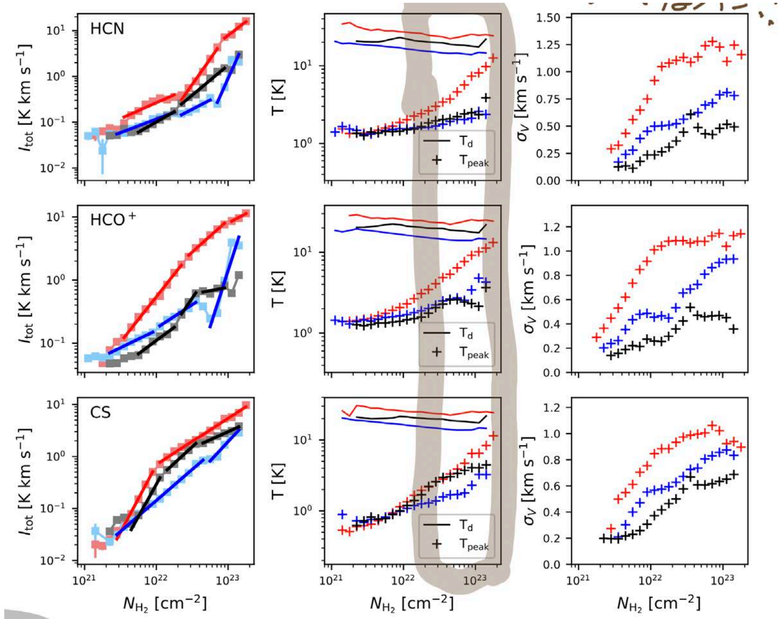

ure 18. Same as Figure 17 but for the HCN (top), HCO$^+$ (middle), and CS (bottom) lines

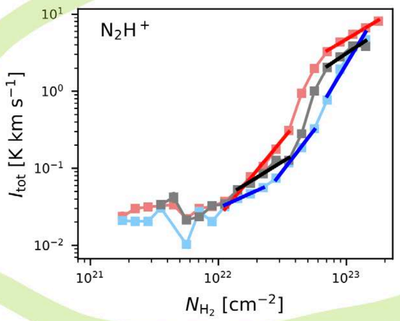

Figure 19. Same as the left panel of Figure 17 but for the N_2H^+ line.

In a companion paper (Yun et al., submitted), we use the TIMES data to explore the relationship between turbulence and star formation activity in MCs. We apply principal component analysis (the PCA; Heyer & Schloerb 1997; Brunt & Heyer 2013), which is one of the statistical methods used to derive the low-order velocity structure function, to the spectral maps presented in this paper. The uniform coverage, sensitivity and range of gas tracers included in the TIMES program are ideal for studying MC kinematics and turbulence.

SFN Letters速報ゼミ

July 15, 2021

古屋 玲

#342 24-28担当

24. **Thermal Wave Instability as an Origin of Gap and Ring Structures in Protoplanetary Disks**
Takahiro Ueda, Mario Flock, Tilman Birnstiel ★ Recent millimeter and infrared observations have shown that gap and

20

25. **Multicolor Variability of Young Stars in the Lagoon Nebula: Driving Causes and Intrinsic Timescales**
Laura Venuti, Ann Marie Cody, Luisa M. Rebull, Giacomo Beccari, Mike Irwin, Sowmya Thanvantri, Steve B. Howell, Geert Barentsen ★ Space observatories have provided unprecedented depictions of the many variability behaviors

09 から 15：やや質量の大きい若い星の時間変動観測, 解析は緻密, 星と円盤がcorotationする半径の質量依存性を明らかにした.

26. **Tree-based solvers for adaptive mesh refinement code FLASH – II: radiation transport module TreeRay**
Richard Wünsch, Stefanie Walch, František Dinnbier, Daniel Seifried, Sebastian Haid, Andre Klepitko, Anthony P. Whitworth, Jan Palouš ★ The treatment of radiative transfer with multiple radiation sources is a critical challenge in

16 から 19：現実的なシュミレーションのために輻射場の取り扱い法を研究：輻射の源が複数の場合かつ広いエネルギー域の計算を可能にした.

27. **No impact of core-scale magnetic field, turbulence, or velocity gradient on sizes of protostellar disks in Orion A**
Hsi-Wei Yen, Bo Zhao, Patrick M. Koch, Aashish Gupta ★ We compared the sizes and fluxes of a sample of protostellar

05 から 08：研究目標はこの分野の最重要課題. 物理的因果関係がないから無相関だったのかもしれないが, 解析の粗さが目立つ, それに起因?

28. **TIMES I: a Systematic Observation in Multiple Molecular Lines Toward the Orion A and Ophiuchus Clouds**
Hyeong-Sik Yun, Jeong-Eun Lee, Yunhee Choi, Neal J. Evans II, Stella S. R. Offner, Mark H. Heyer, Brandt A. L. Gaches, Yong-Hee Lee, Giseon Baek, Minho Choi, Hyunwoo Kang, Seokho Lee, Ken'ichi Tatematsu, Yao-Lun Yang, How-Huan Chen, Youngung Lee, Jae Hoon Jung, Changhoon Lee, Jungyeon Cho ★ We have

01 から 04：オリオン南部を含めたおそらく始めての多輝線観測. 基本的なデータの提示論文.
だが堅実な解析, 続編を大いに期待.

27. **No impact of core-scale magnetic field, turbulence, or velocity gradient on sizes of protostellar disks in Orion A**

Hsi-Wei Yen, Bo Zhao, Patrick M. Koch, Aashish Gupta ★ We compared the sizes and fluxes of a sample of protostellar

ABSTRACT

We compared the sizes and fluxes of a sample of protostellar disks in Orion A measured with the ALMA 0.87 mm continuum data from the VANDAM survey with the physical properties of their ambient environments on the core scale of 0.6 pc estimated with the GBT GAS NH_3 and JCMT SCUPOL polarimetric data. We did not find any significant dependence of the disk radii and continuum fluxes on a single parameter on the core scale, such as the non-thermal line width, magnetic field orientation and strength, or magnitude and orientation of the velocity gradient. Among these parameters, we only found a positive correlation between the magnitude of the velocity gradient and the non-thermal line width. Thus, the observed velocity gradients are more likely related to turbulent motion but not large-scale rotation. Our results of no clear dependence of the disk radii on these parameters are more consistent with the expectation from non-ideal MHD simulations of disk formation in collapsing cores, where the disk size is self-regulated by magnetic braking and diffusion, compared to other simulations which only include turbulence and/or a magnetic field misaligned with the rotational axis. Therefore, our results could hint that the non-ideal MHD effects play a more important role in the disk formation. Nevertheless, we cannot exclude the influences on the observed disk size distribution by dynamical interaction in a stellar cluster or amounts of angular momentum on the core scale, which cannot be probed with the current data.

Keywords: Star formation (1569), Interstellar magnetic fields (845), Star forming regions (1565), Protostars (1302), Circumstellar disks (235)

3.1. *ALMA 0.87 mm continuum*

sists of 328 protostellar sources. The ALMA observations of the VANDAM survey are conducted at 0.87 mm and have a synthesized beam of 0.″11, corresponding to 39–49 au at the distances to Orion A and B. The Orion A molecular clouds

3.2. *GBT NH_3 emission*

32″, corresponding to 11 000–14 000 au at the distances to Orion A and B.

3.3. *JCMT polarized 850 μm continuum*

For the 34 protostars with more than three nearby polarization detections within 15″, we also measured its angle dispersion of the magnetic field orientations on the core scale of 0.06 pc. To remove contributions by large-scale magnetic field structures, we adopted the method similar to unsharp masking, as introduced in, for example, Pattle et al. (2017) and Wang, J.-W. et al. (2019). For each polarization detection within 15″ from a sample protostar, we computed the mean Stokes Q and U intensities and thus the mean polarization orientation of 3 by 3 pixels centered at that detection, which is assumed to be the large-scale magnetic field orienta-

2. SAMPLE

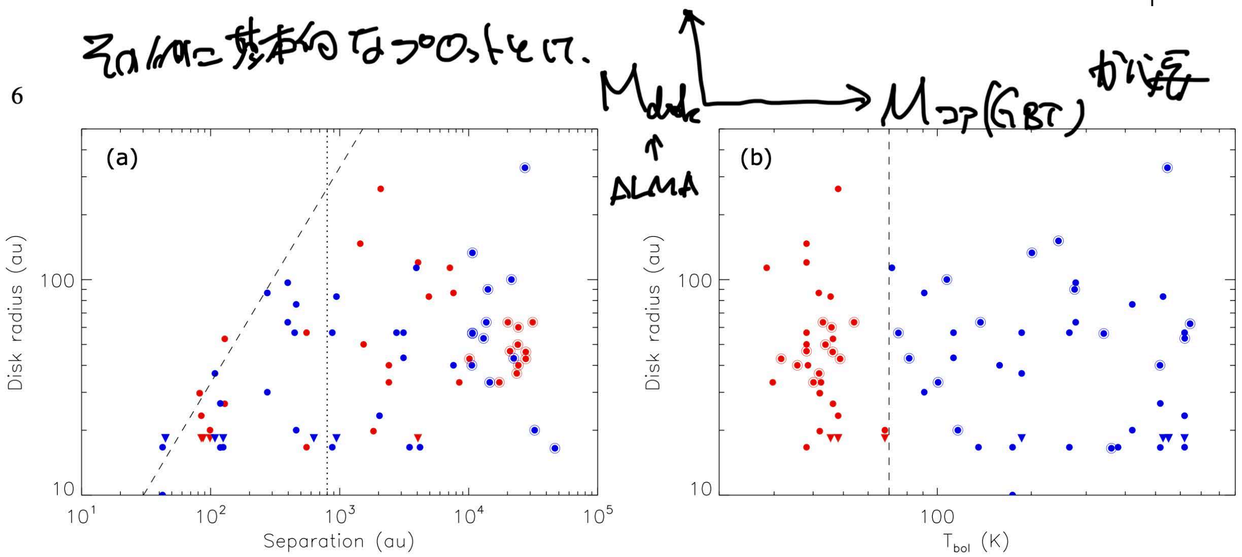

Figure 2. Comparisons between the disk radii measured with the ALMA 0.87 mm continuum data and (a) the projected separations and (b) the bolometric temperatures of the protostars. If the disks are not resolved with the synthesized beam of 0.″11 (43 au), the upper limits of their radii are plotted as triangles. Red dots are the Class 0 protostars, and blue dots are Class I and flat-spectrum protostars. For a given protostar, the separation is defined as its distance to the protostar nearest to it. Single protostars are also plotted here with the separations calculated with the same definition, and they are labelled with open circles. In (a), a dashed line presents the expected truncation radius as a function of separation in a binary system with equal masses and a non-eccentric binary orbit, and a vertical dotted line denotes a separation of 800 au. In (b), a vertical dashed line denotes a bolometric temperature of 70 K, which is adopted to separate Class 0 and more evolved protostars.

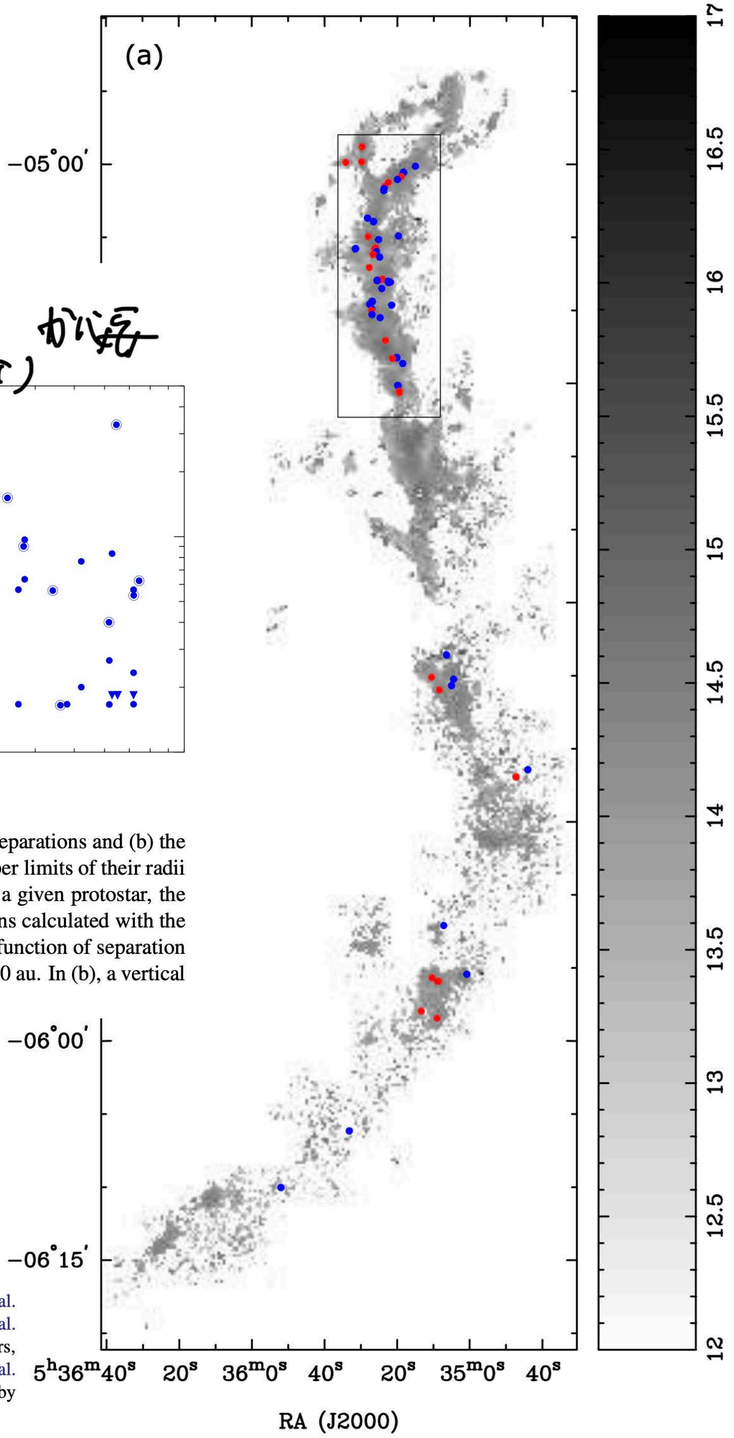

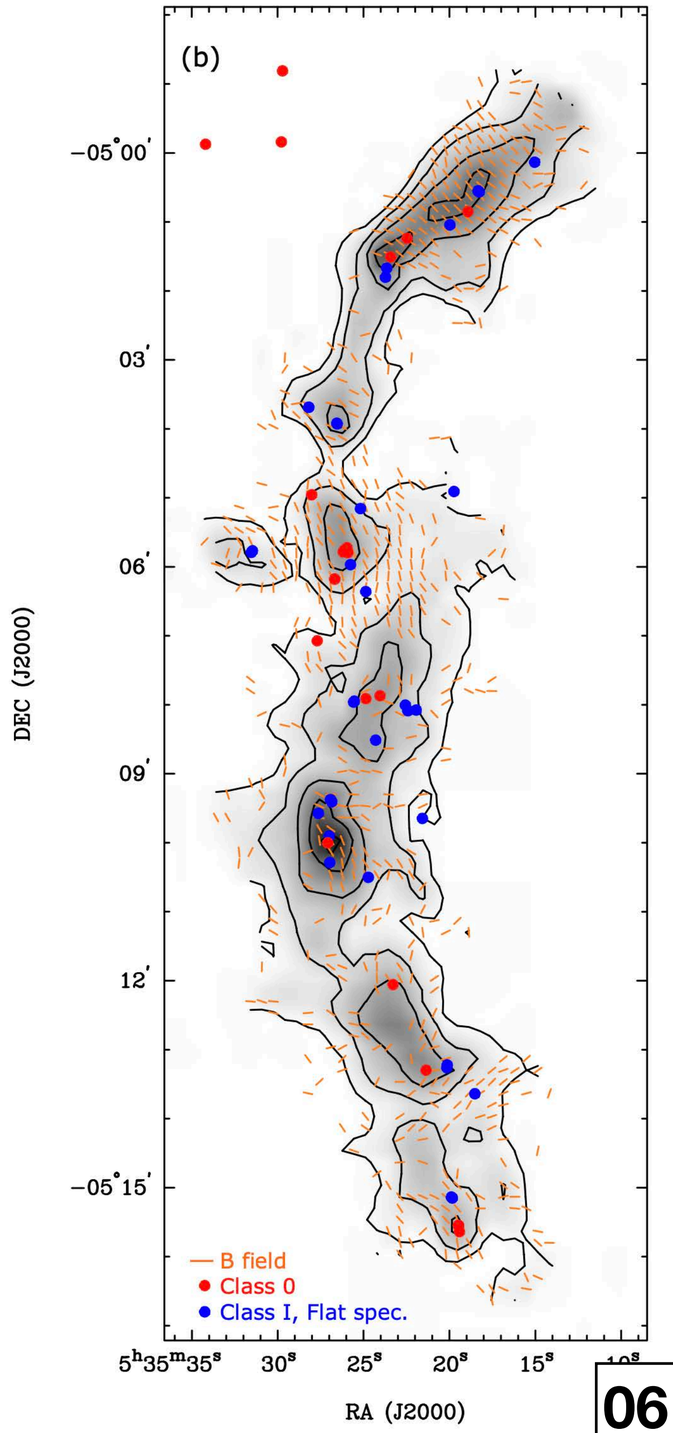

Figure 1. (a) NH_3 column density map in a logarithmic scale of Orion A obtained by the Green Bank Ammonia Survey (GAS; Friesen et al. 2017; Kirk et al. 2017). Red and blue dots show the locations of our sample protostars selected from the VANDAM survey of Orion (Tobin et al. 2019, 2020). A bolometric temperature of 70 K was adopted to separate Class 0 and more evolved protostars. Red dots are the Class 0 protostars, and blue dots are the Class I and flat-spectrum protostars. A rectangle denotes the mapping area of the JCMT SCUPOL survey (Matthews et al. 2009). (b) 850 μm intensity map obtained with the JCMT SCUPOL survey. Orange segments show the magnetic field orientations inferred by rotating the polarization orientations by 90°. Red and blue dots are the same as those in (a).

4. RESULTS

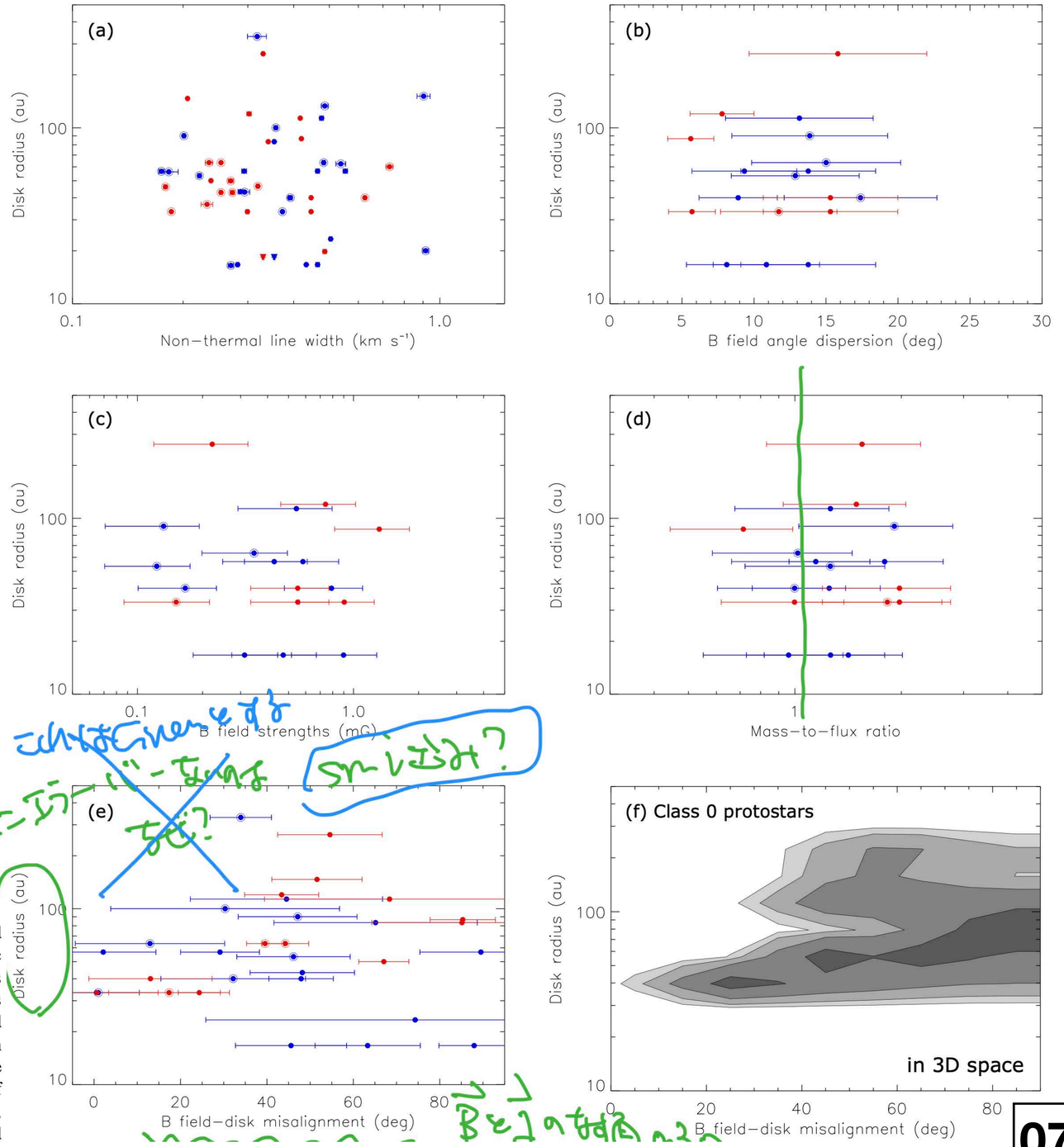

Figure 3. Comparisons between the disk radii measured with the ALMA 0.87 mm continuum data and (a) the non-thermal line widths measured with the GBT NH_3 data, (b) the angular dispersions of the magnetic field orientations measured with the JCMT SCUPOL data, (c) the magnetic field strengths estimated with the Davis–Chandrasekhar–Fermi method, (d) the normalized mass-to-flux ratios, and (e) the misalignments between the rotational axes of the disks and the magnetic fields projected on the plane of the sky, on the core scale of 0.06 pc. Error bars present the 1σ uncertainties. If the disks are not resolved with the synthesized beam of 0.″11 (43 au), the upper limits of their radii are plotted as triangles. Red dots are the Class 0 protostars, and blue dots are Class I and flat-spectrum protostars. Single protostars are labelled with open circles. (f) Inferred probability distribution of the 3D misalignments between the rotational axes of the disks and the magnetic fields for the Class 0 protostars in (e). The distribution was sampled with bin sizes of the disk radii in a logarithm scale from 1.45 in steps of 0.075 in units of au and the 3D misalignment angles in a linear scale from 0° in steps of 10°. The probabilities to have a data point within the innermost, second, third, and outermost contours are 35%, 81%, 96%, and 98%, respectively, where the probability is computed as the number of the simulated data points enclosed by a given contour divided by the total number of all the data points.

4. RESULTS

5. DISCUSSION

5.1. *Effects of turbulence and magnetic field*

5.2. *Effects of large-scale motions*

5.3. *Effects of crowded environments*

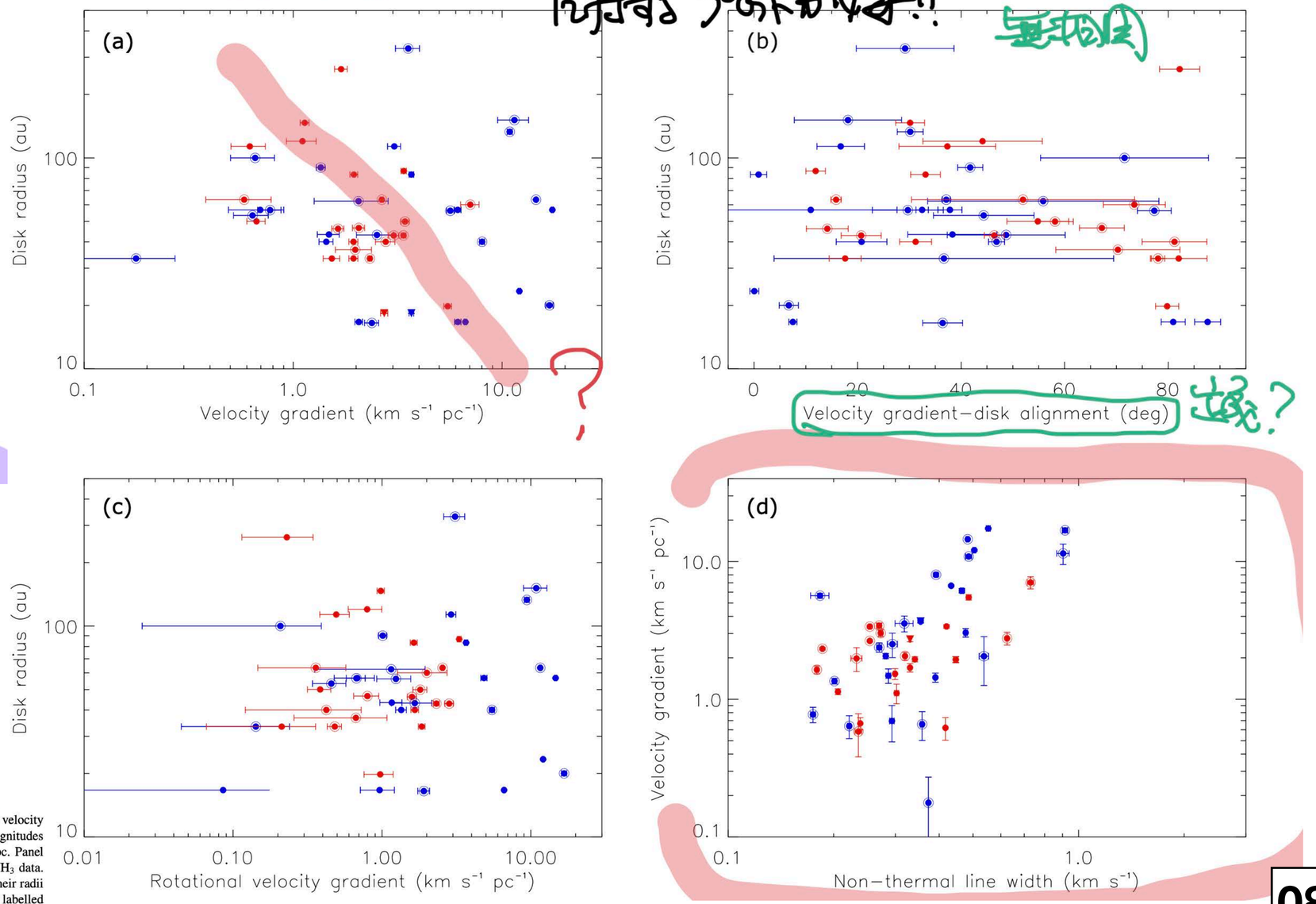

Figure 4. Comparisons between the disk radii measured with the ALMA 0.87 mm continuum data and (a) the magnitudes of the velocity gradients measured with the GBT NH_3 data, (b) the alignments between the disk major axes and the velocity gradients, and (c) the magnitudes of the velocity gradients projected onto the disk major axes as an assessment of possible rotational motion, on the core scale of 0.06 pc. Panel (d) compares the magnitudes of the velocity gradients with the non-thermal line widths on the core scale measured with the GBT NH_3 data. Error bars present the 1σ uncertainties. If the disks are not resolved with the synthesized beam of 0.″11 (43 au), the upper limits of their radii are plotted as triangles. Red dots are the Class 0 protostars, and blue dots are Class I and flat-spectrum protostars. Single protostars are labelled with open circles.

SFN Letters速報ゼミ

July 15, 2021

古屋 玲

#342 24-28担当

24. **Thermal Wave Instability as an Origin of Gap and Ring Structures in Protoplanetary Disks**
Takahiro Ueda, Mario Flock, Tilman Birnstiel ★ Recent millimeter and infrared observations have shown that gap and

20

25. **Multicolor Variability of Young Stars in the Lagoon Nebula: Driving Causes and Intrinsic Timescales**
Laura Venuti, Ann Marie Cody, Luisa M. Rebull, Giacomo Beccari, Mike Irwin, Sowmya Thanvantri, Steve B. Howell, Geert Barentsen ★ Space observatories have provided unprecedented depictions of the many variability behaviors

09 から 15：やや質量の大きい若い星の時間変動観測, 解析は緻密, 星と円盤がcorotationする半径の質量依存性を明らかにした.

26. **Tree-based solvers for adaptive mesh refinement code FLASH – II: radiation transport module TreeRay**
Richard Wünsch, Stefanie Walch, František Dinnbier, Daniel Seifried, Sebastian Haid, Andre Klepitko, Anthony P. Whitworth, Jan Palouš ★ The treatment of radiative transfer with multiple radiation sources is a critical challenge in

16 から 19：現実的なシュミレーションのために輻射場の取り扱い法を研究：輻射の源が複数の場合かつ広いエネルギー域の計算を可能にした.

27. **No impact of core-scale magnetic field, turbulence, or velocity gradient on sizes of protostellar disks in Orion A**
Hsi-Wei Yen, Bo Zhao, Patrick M. Koch, Aashish Gupta ★ We compared the sizes and fluxes of a sample of protostellar

05 から 08：研究目標はこの分野の最重要課題. 物理的因果関係がないから無相関だったのかもしれないが, 解析の粗さが目立つ, それに起因?

28. **TIMES I: a Systematic Observation in Multiple Molecular Lines Toward the Orion A and Ophiuchus Clouds**
Hyeong-Sik Yun, Jeong-Eun Lee, Yunhee Choi, Neal J. Evans II, Stella S. R. Offner, Mark H. Heyer, Brandt A. L. Gaches, Yong-Hee Lee, Giseon Baek, Minho Choi, Hyunwoo Kang, Seokho Lee, Ken'ichi Tatematsu, Yao-Lun Yang, How-Huan Chen, Youngung Lee, Jae Hoon Jung, Changhoon Lee, Jungyeon Cho ★ We have

01 から 04：オリオン南部を含めたおそらく始めての多輝線観測. 基本的なデータの提示論文.
だが堅実な解析, 続編を大いに期待.

25. **Multicolor Variability of Young Stars in the Lagoon Nebula: Driving Causes and Intrinsic Timescales**

Laura Venuti, Ann Marie Cody, Luisa M. Rebull, Giacomo Beccari, Mike Irwin, Sowmya Thanvantri, Steve B. Howell, Geert Barentsen ★ Space observatories have provided unprecedented depictions of the many variability behaviors

ABSTRACT

Space observatories have provided unprecedented depictions of the many variability behaviors typical of low-mass, young stars. However, those studies have so far largely omitted more massive objects ($\sim$2 $M_\odot$ to 4–5 $M_\odot$), and were limited by the absence of simultaneous, multi-wavelength information. We present a new study of young star variability in the $\sim$1–2 Myr-old, massive Lagoon Nebula region. Our sample encompasses 278 young, late-B to K-type stars, monitored with *Kepler/K2*. Auxiliary $u, g, r, i, H\alpha$ time series photometry, simultaneous with *K2*, was acquired at the Paranal Observatory. We employed this comprehensive dataset and archival infrared photometry to determine individual stellar parameters, assess the presence of circumstellar disks, and tie the variability behaviors to inner disk dynamics. We found significant mass-dependent trends in variability properties, with B/A stars displaying substantially reduced levels of variability compared to G/K stars for any light curve morphology. These properties suggest different magnetic field structures at the surface of early-type and later-type stars. We also detected a dearth of some disk-driven variability behaviors, particularly dippers, among stars earlier than G. This indicates that their higher surface temperatures and more chaotic magnetic fields prevent the formation and survival of inner disk dust structures co-rotating with the star. Finally, we examined the characteristic variability timescales within each light curve, and determined that the day-to-week timescales are predominant over the *K2* time series. These reflect distinct processes and locations in the inner disk environment, from intense accretion triggered by instabilities in the innermost disk regions, to variable accretion efficiency in the outer magnetosphere.

Keywords: Young stellar objects (1834), Circumstellar disks (235), Variable stars (1761), Young star clusters (1833), Multi-color photometry (1077), Time series analysis (1916)

1. INTRODUCTION

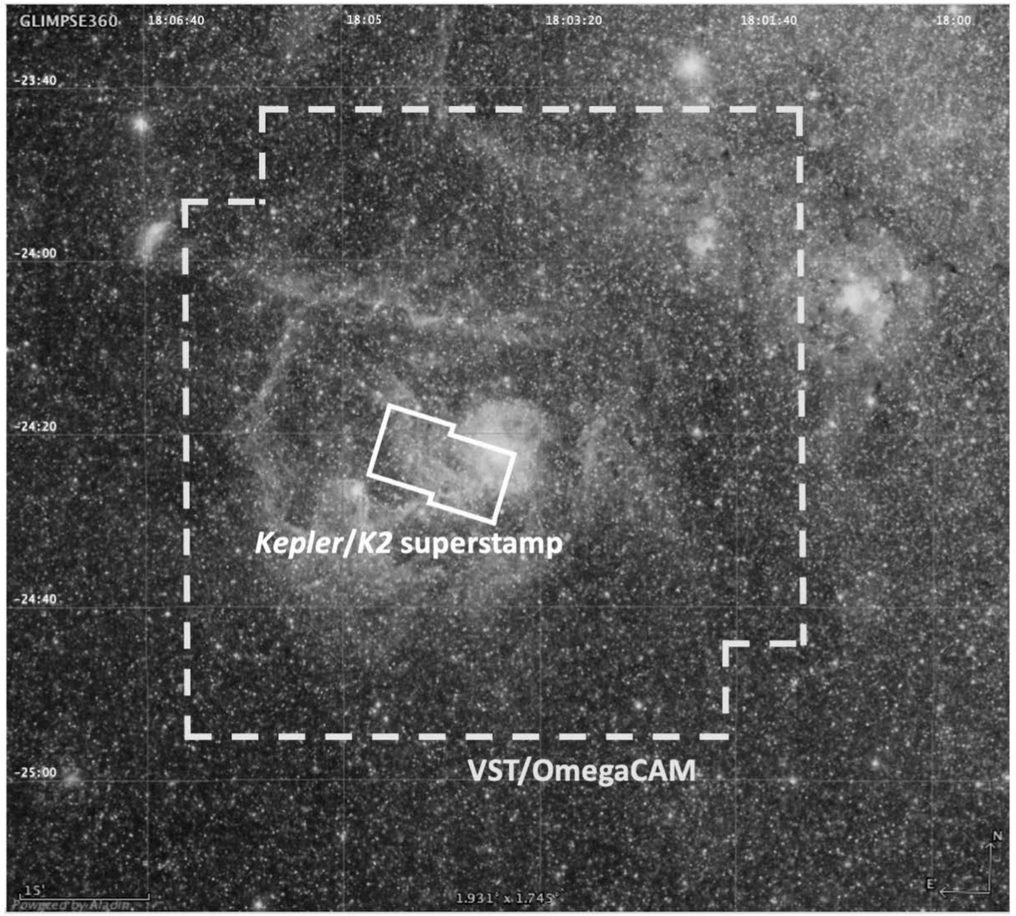

Figure 1. Black and white image of the Lagoon Nebula field from *Spitzer*/GLIMPSE, over which the total area covered with VST/OmegaCAM (sum of two dithered pointings) and the *Kepler*/*K2* superstamp region are outlined as dashed and solid contours, respectively. The original version of the background image was prepared with Aladin Desktop (Bonnarel et al. 2000).

K2 monitored the Lagoon Nebula from April 21 through July 1, 2016.

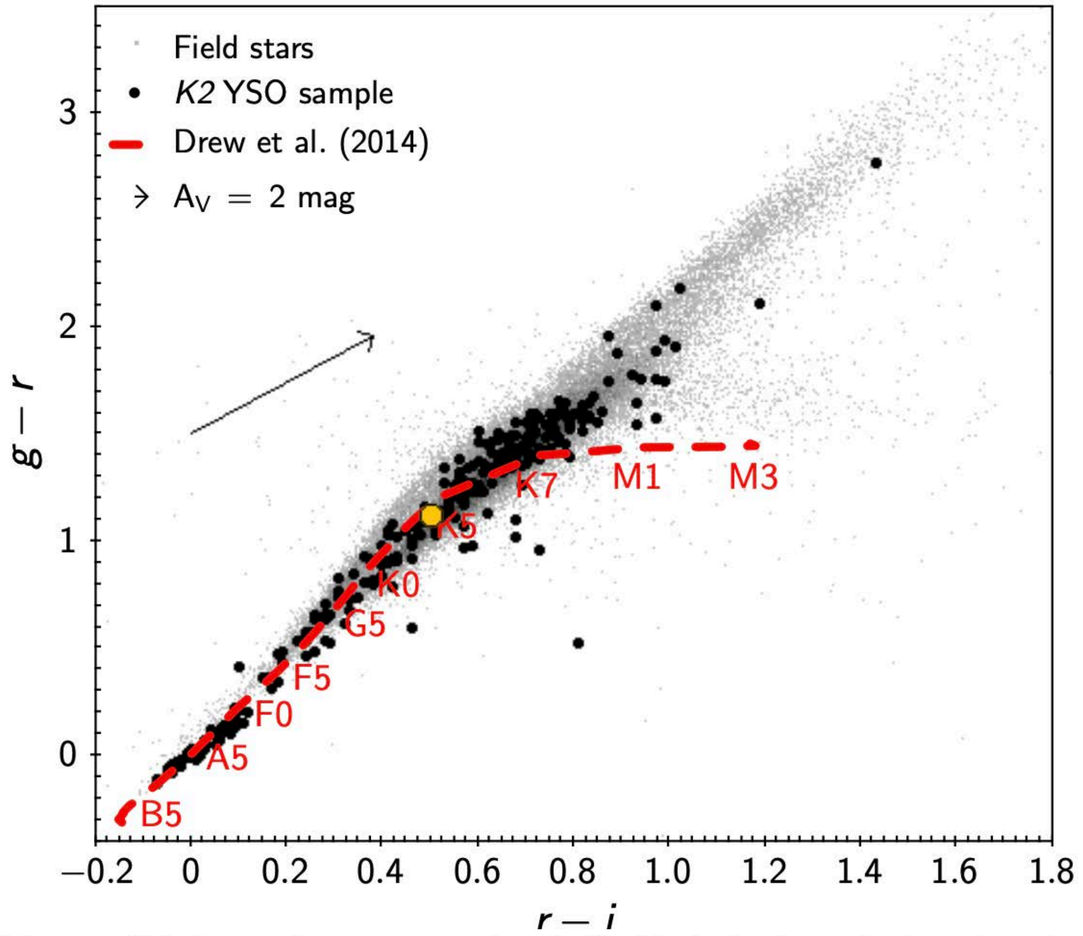

Figure 3. *Left:* Typical VST g, r, i colors of Lagoon Nebula members monitored with *K2* (black dots), overlaid on the color distribution of field stars (gray dots). The sequence of synthetic, non-reddened colors tabulated in Drew et al. (2014) is dashed in red as a reference, and the location of representative SpTs is labelled along the sequence to guide the reader. The extinction vector shown on the diagram corresponds to $A_V = 2$ mag following a non-standard reddening law with $R_V = 5$. A yellow dot marks the object for which results of the A_V derivation are shown as an example in the right panel. *Right*: Average A_V measured from $r - i$ and $g - r$ colors, and absolute difference between the corresponding $A_V\,(r-i)$ and $A_V\,(g-r)$, calculated for the object marked in yellow on the left panel with respect to the non-reddened colors tabulated for each SpT in Drew et al. (2014), and labeled as a reference along the A_V curve. The spectral type that minimizes the difference $|A_V\,(g-r) - A_V\,(r-i)|$ is extracted as best SpT estimate, and the corresponding average $< A_V\,(g,r,i) >$ is extracted as best estimate of individual A

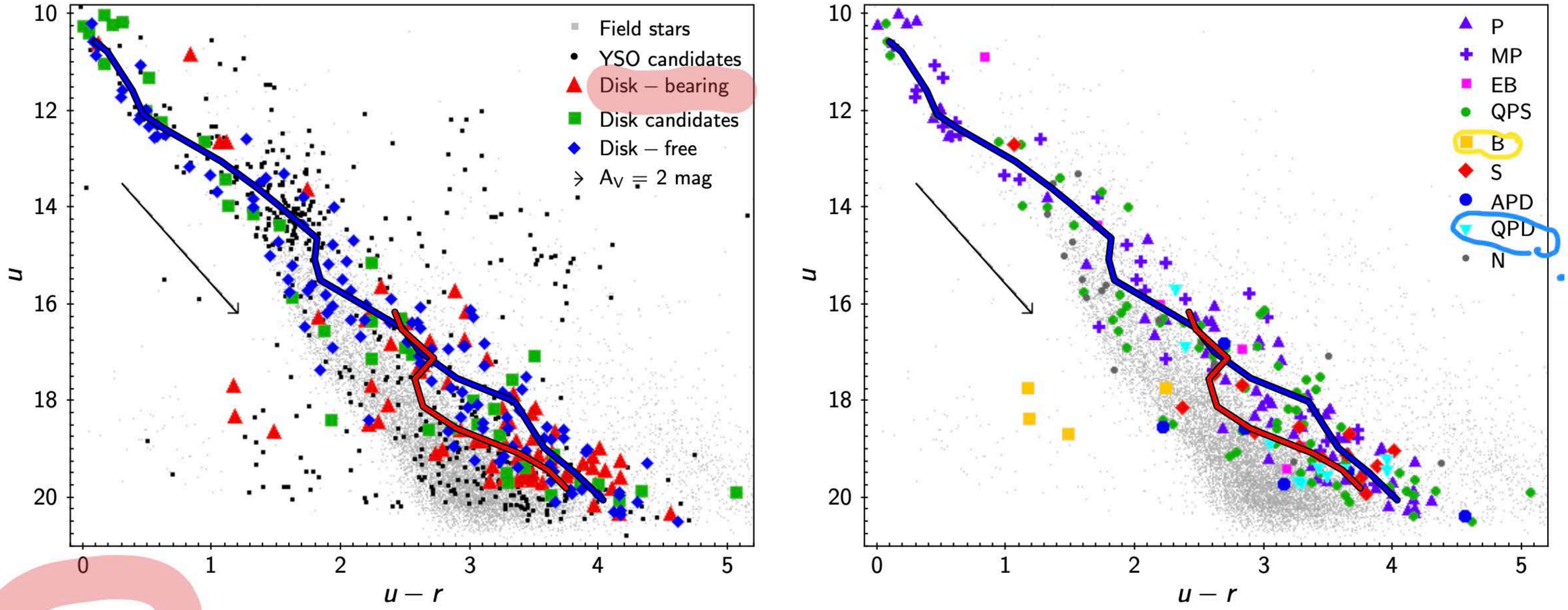

Figure 9. *Left*: $(u - r,\ u)$ color-magnitude diagram for stars in the Lagoon Nebula field surveyed with VST/OmegaCAM. Gray dots correspond to field stars, black dots to YSO candidates in the field. Red triangles, green squares, and blue diamonds correspond respectively to disk–bearing, disk candidate, and disk–free Lagoon Nebula members monitored with *K2*. The blue curve and the red curve trace respectively the average $u - r$ colors measured as a function of u-band magnitude for disk–free (Class III) and disk–bearing (Class II) objects. The reddening vector on the left of the diagram traces the photometric shift induced by a 2 mag extinction according to a reddening law with $R_V = 5$. *Right*: Same diagram as in the left panel, with *K2* Lagoon Nebula YSOs sorted according to their light curve morphology. Colors and symbols are associated with different variability classes following the same convention as in Fig. 6. Non–variable stars (i.e., flat–line light curves) are indicated as charcoal-gray dots.

- *periodic* (P), which exhibit repeated, sinusoidal-like flux patterns with little or no evolution in shape or amplitude from one cycle to the next;
- *quasi-periodic symmetric* (QPS), which exhibit an overall periodic flux pattern, symmetric in amplitude below and above the typical luminosity level of the star, but with noticeable changes in shape and/or amplitude from one cycle to the next;
- *stochastic* (S), which exhibit irregular flux variations with no apparent periodicity and no preference for brightening events over fading events or vice versa;
- *bursters* (B), which exhibit irregular flux variations, prominently in the form of intense and short–lived brightening events on top of a flat or slowly–varying light curve continuum, occurring with no obvious periodicity but repeatedly over spans of days or weeks;
- *quasi-periodic dippers* (QPD), which exhibit prominent fading events, in a recurring pattern with a detectable periodicity, although with changes in shape and depth from one cycle to the next;
- *aperiodic dippers* (APD), which exhibit prominent fading events, possibly repeated but with no obvious periodicity along the time series;
- *multi-periodic* (MP), which exhibit multiple periodicities (e.g., a beating pattern or pulsations);
- *eclipsing binaries* (EB), which exhibit the characteristic photometric signatures of one companion transiting the other, superimposed on the out–of–eclipse individual variability patterns.

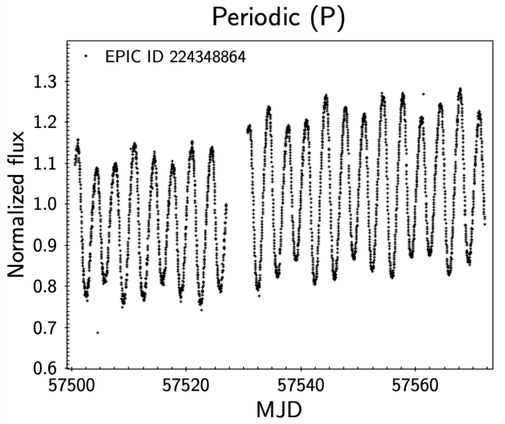

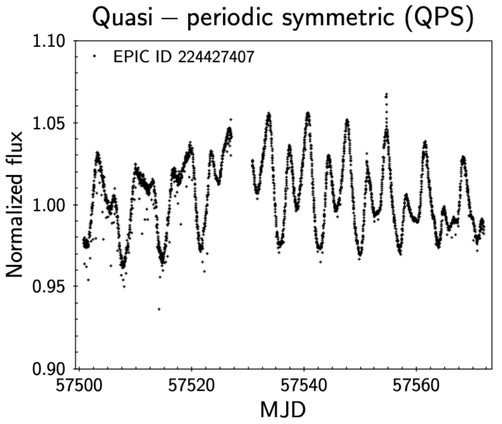

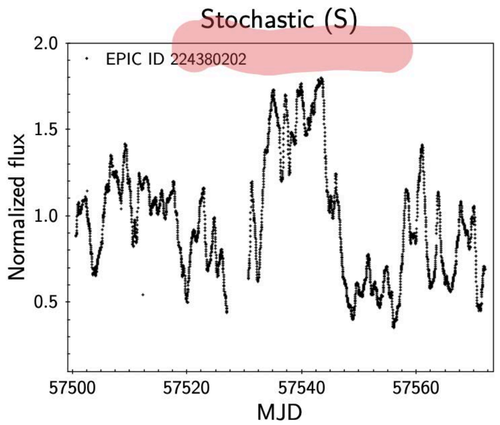

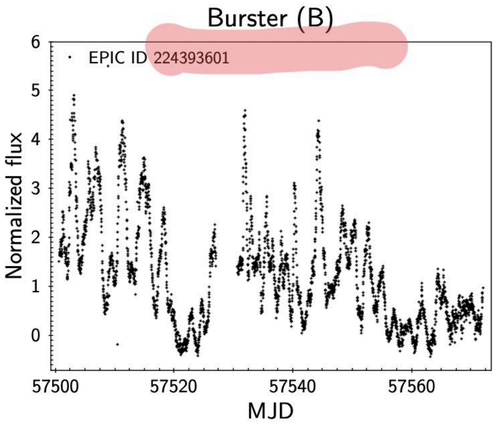

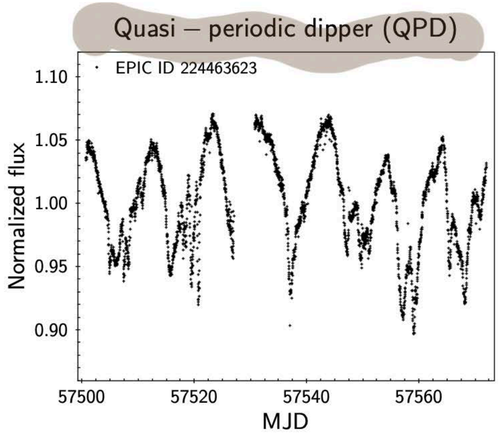

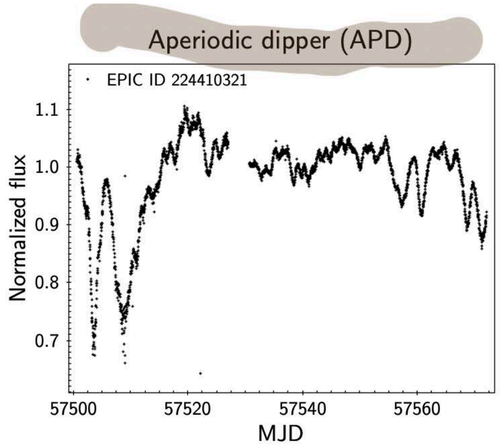

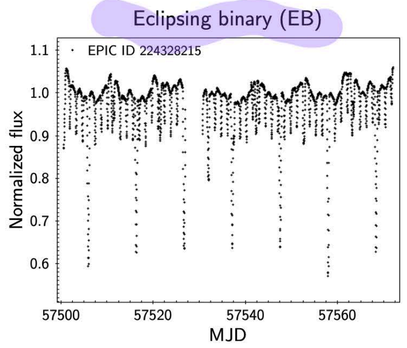

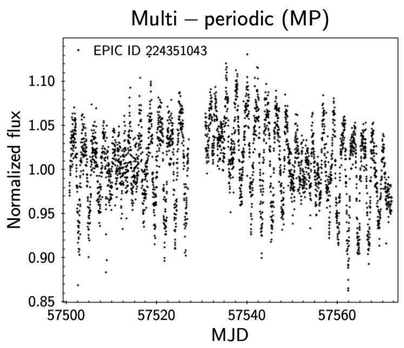

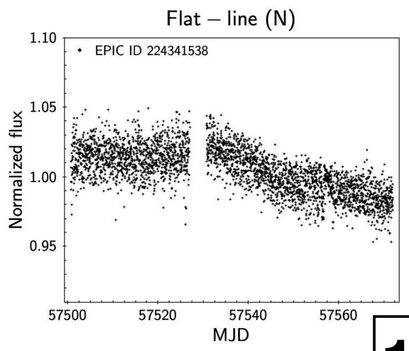

4.2. *Multiwavelength correlated variability from VST/OmegaCAM data*

To assess the amount of intrinsic variability, beyond the photometric noise level, among Lagoon Nebula members, we implemented the variability index $\mathcal{J}$ defined in Stetson (1996). The $\mathcal{J}$ index measures the amount of correlated variability observed for a given star at two different wavelengths m and m':

$$\mathcal{J} = \frac{\sum_{k=1}^{n} w_k \, \mathrm{sgn}\,(P_k) \sqrt{|P_k|}}{\sum_{k=1}^{n} w_k}, \tag{4}$$

where n is the number of time-ordered observations, $P_k = \frac{n}{n-1}\left(\frac{m_k - \overline{m}}{\sigma_m}\right)\left(\frac{m'_k - \overline{m'}}{\sigma_{m'}}\right)$, $\mathrm{sgn}\,(P_k)$ takes value +1 if P_k is positive and -1 if P_k is negative, m_k and m'_k are the magnitudes measured during the k^{th} observing epoch, $\overline{m}$ and

6. TIMESCALES OF VARIABILITY FROM *K2* LIGHT CURVES

In order to probe the characteristic timescales of variability of Lagoon Nebula members, irrespective of the periodic or aperiodic nature of their variation patterns, we adopted the method of structure functions (Simonetti et al. 1985; Hughes et al. 1992; de Vries et al. 2003), as recently implemented to study YSO variability by Sergison et al. (2020). The method consists of extracting every timescale of variability τ encompassed by the time series, and, for each τ, computing the average amplitude of normalized flux variability among all pairs of points in the light curve that are spaced by that time interval τ. The structure function ($\mathcal{SF}$) is then defined as the average variability amplitude measured within the light curve as a function of τ. In order to apply the $\mathcal{SF}$ method to a discrete time series, with possibly unevenly spaced data, we first identify the range of investigated τ, from τ_{min} (i.e., the minimum timescale of variability that can be reliably extracted from the light curve) to τ_{max} (i.e., the maximum timescale of variability that can be reliably extracted from the light curve). We then divide this (τ_{min}, τ_{max}) range into logarithmically spaced timescale bins, and, for each bin (τ_1, τ_2), we select all pairs of light curve epochs (t_i, t_j), where $j > i$ and $\tau_1 < t_j - t_i < \tau_2$. The average variation in normalized flux, measured across all pairs of selected points, defines the value of $\mathcal{SF}(\tau_1, \tau_2)$ as

$$\mathcal{SF}(\tau_1, \tau_2) = \sqrt{\frac{1}{N(\tau_1, \tau_2)} \sum_{j>i} (f_i - f_j)^2}, \tag{5}$$

where $N(\tau_1, \tau_2)$ is the number of pairs of light curve points (i, j) separated in time by an amount comprised between τ_1 and τ_2, and f_i is the normalized flux measured at time t_i.

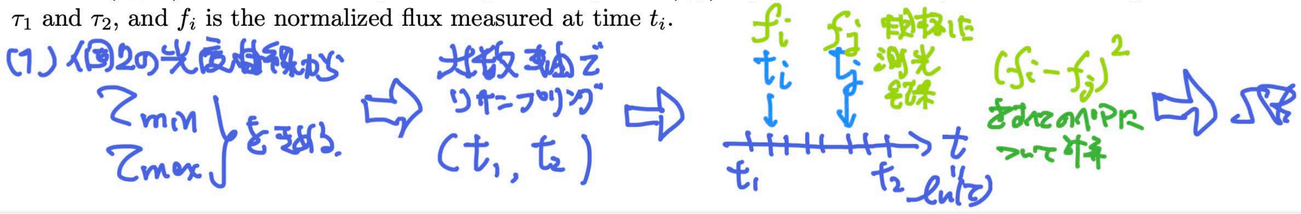

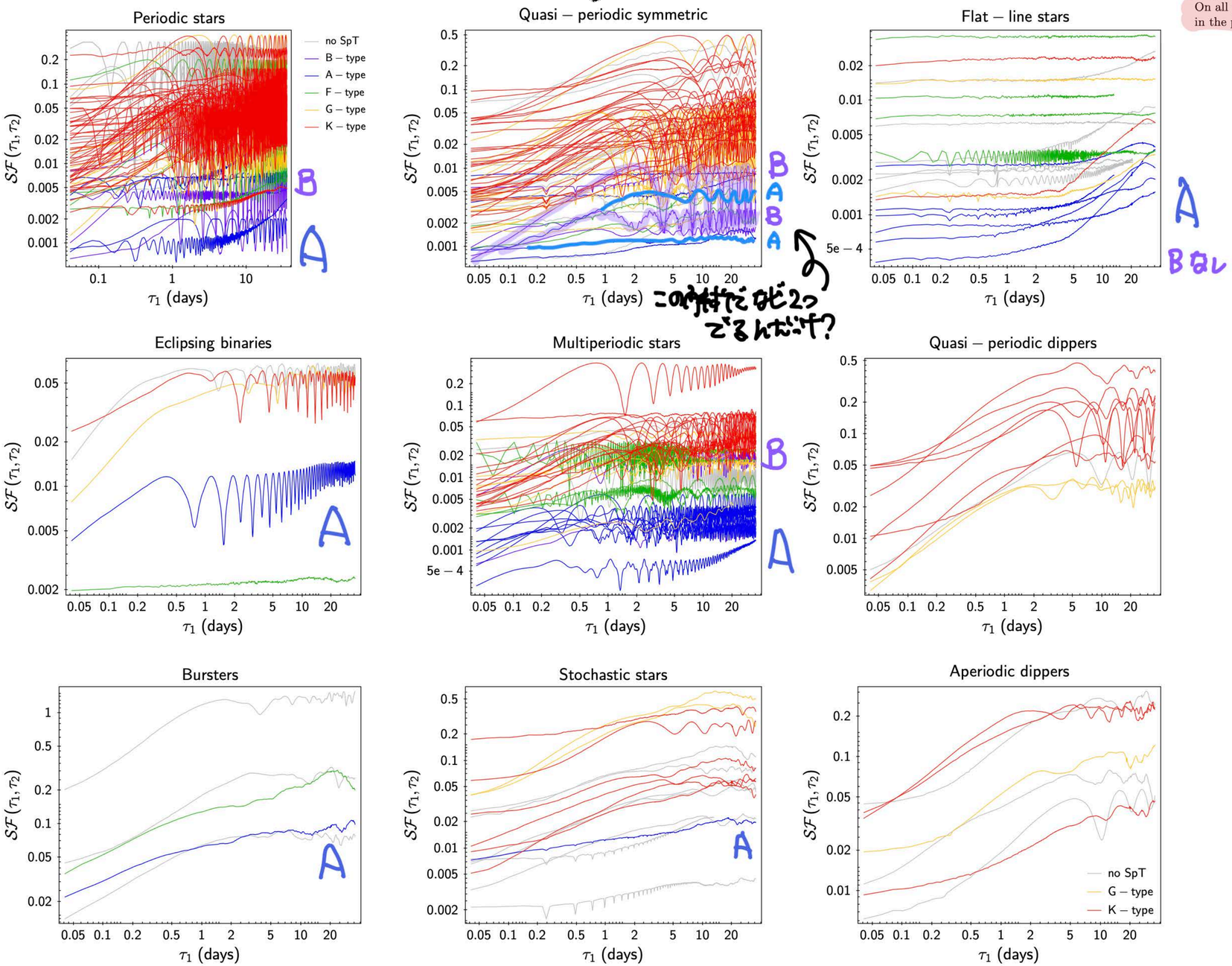

Figure 12. Structure functions $\mathcal{SF}$ computed for each *K2* light curve on timescales τ ranging from twice the data cadence to half the light curve span, sampled as discussed in Sect. 6. For each bin (τ_1, τ_2) of investigated variability timescales, the value of $\mathcal{SF}$ resulting from Eq. 5 is plotted as a function of τ_1 for illustration purposes. Each class of light curve variability is shown in a different panel, as indicated on top of each diagram (the 'U' class described in Sect. 4.1 is not included here). Different colors identify different SpT, as detailed to the right of the top left panel (purple → B–type stars; blue → A–type stars; green → F–type stars; yellow → G–type stars; red → K–type stars; gray → stars with no SpT estimate from the procedure in Sect. 3.1). On all panels, it is possible to observe a systematic increase of the intrinsic variability amplitude (as traced by the value of $\mathcal{SF}$ in the plateau region at large timescales) from earlier-type stars to later-type stars.

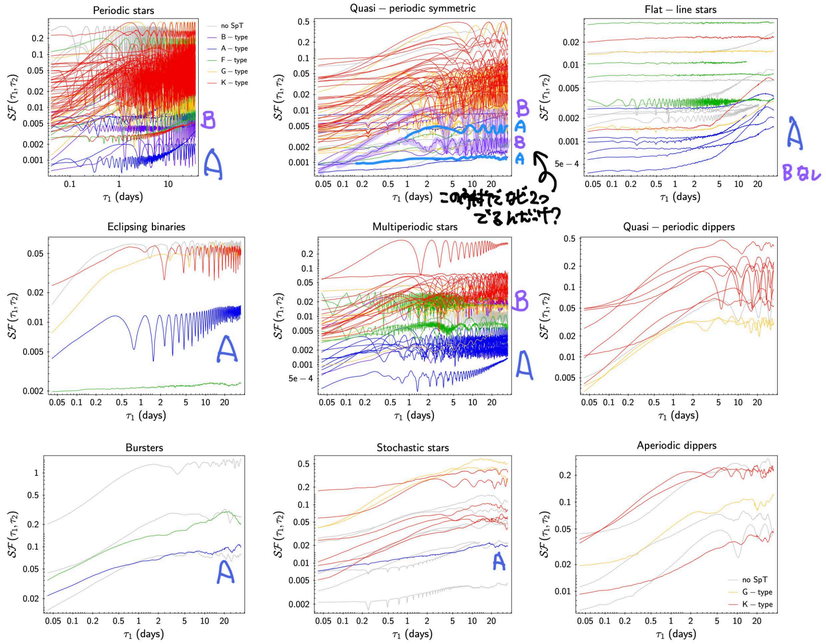

7. DISCUSSION

7.1. *Mass dependence of variability in young stars*

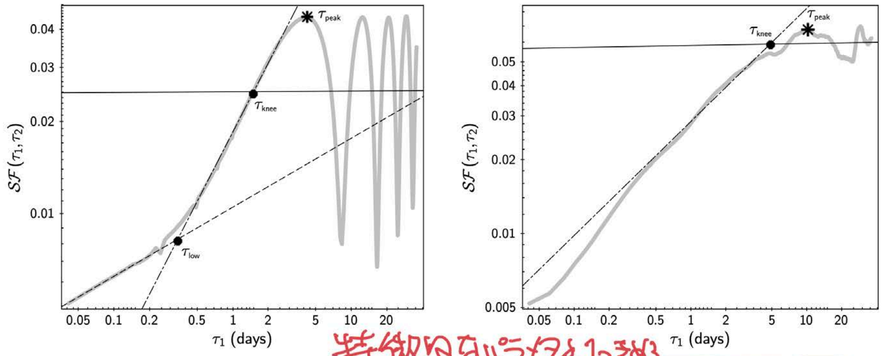

Figure 13. Examples of $\mathcal{SF}$ analysis conducted on *K2* light curves to extract the characteristic timescales of variability. The $\mathcal{SF}$ shown in gray on the left belongs to the K–type star EPIC ID 224438171, whose variability behavior is classified as P, while the one shown on the right belongs to the K–type star EPIC ID 224337699, classified as S. The dashed black line traces the best power-law fit derived for the first $\mathcal{SF}$ regime (τ range where the photometric noise is predominant; not observed in the second case). The dash-dotted black line traces the best power-law fit derived for the main $\mathcal{SF}$ regime (τ range dominated by intrinsic variability on the corresponding timescales). The solid black line traces the best power-law fit to the third $\mathcal{SF}$ regime (τ range where the observed variability is a reflection of the variability observed on shorter timescales). The timescales of intersection between first-regime and second-regime fits (τ_{low}), and between second-regime and third-regime fits (τ_{knee}) are marked as large black dots. The asterisk marks the timescale corresponding to the first observed maximum in the $\mathcal{SF}$ (τ_{peak}). The small negative spikes, visible in the $\mathcal{SF}$ on the left at $\tau \sim 0.24$ d, 0.49 d, and repeatedly after that, are spurious features induced by the corrective thruster firings operated roughly every six hours during the *K2* mission (Howell et al. 2014).

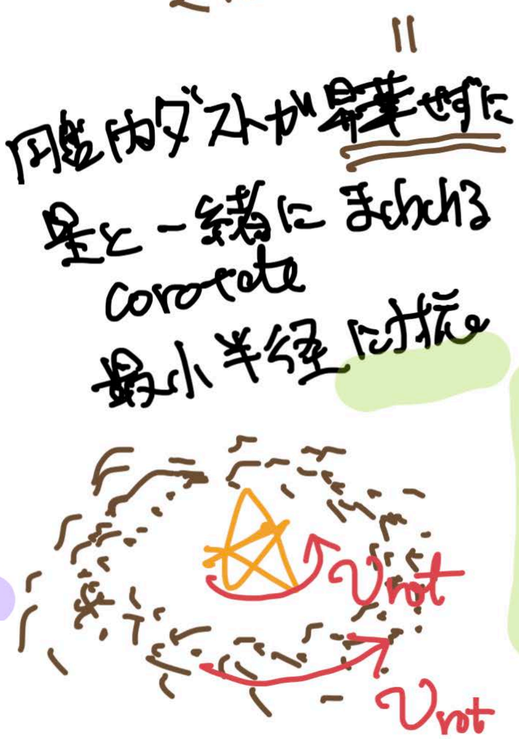

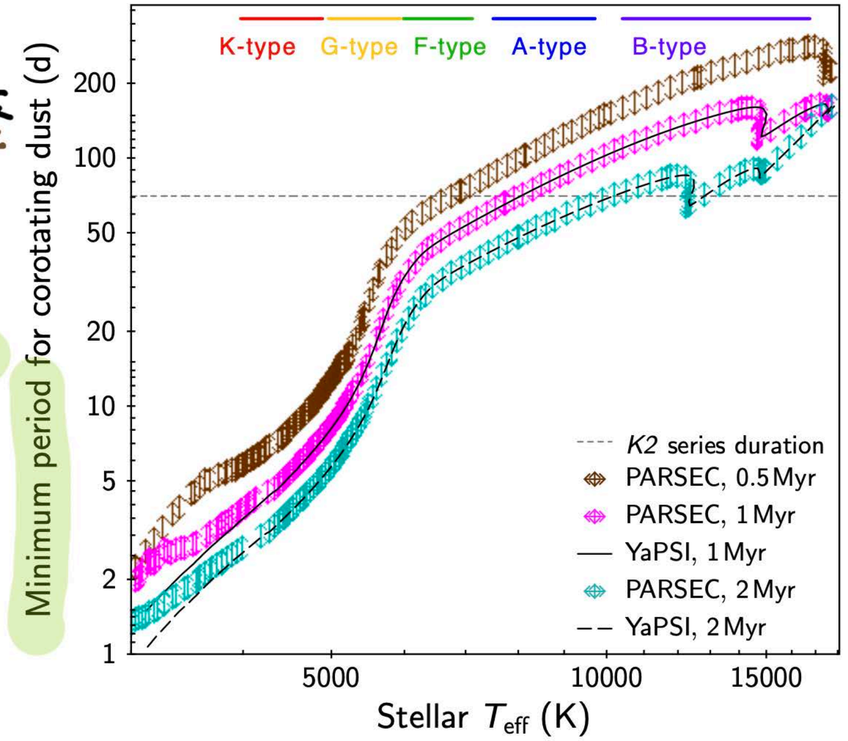

Figure 14. Estimates of the orbital period corresponding to the minimum radial distance from the star at which corotating dust can be present in non-sublimated form, as a function of the temperature of the central star. The double-arrows delimit the range of periods calculated, for a given $T_{\rm eff}$, assuming a dust sublimation temperature of 1300–1400 K, and using stellar parameters (mass, luminosity) tabulated by Marigo et al. (2017, PARSEC isochrones) for 0.5 Myr (brown), 1 Myr (magenta), and 2 Myr (cyan) ages. The average $T_{\rm eff}$–period estimates derived by using Spada et al.'s (2017, YaPSI) model isochrones at 1 Myr (solid line) and 2 Myr (dashed line) are also shown to illustrate the overall agreement between different PMS models as a function of stellar $T_{\rm eff}$. The total duration of the *K2* time series is shown for comparison purposes as a dotted gray line. Horizontal bars on top of the diagram illustrate the approximate $T_{\rm eff}$ ranges for stars in our sample belonging to different spectral classes.

7.2. *Geometries of star-disk interaction in young stars*

7.3. *Stability of the different modes of YSO variability*

SFN Letters速報ゼミ

July 15, 2021

古屋 玲

#342 24-28担当

24. **Thermal Wave Instability as an Origin of Gap and Ring Structures in Protoplanetary Disks**
Takahiro Ueda, Mario Flock, Tilman Birnstiel ★ Recent millimeter and infrared observations have shown that gap and

20

25. **Multicolor Variability of Young Stars in the Lagoon Nebula: Driving Causes and Intrinsic Timescales**
Laura Venuti, Ann Marie Cody, Luisa M. Rebull, Giacomo Beccari, Mike Irwin, Sowmya Thanvantri, Steve B. Howell, Geert Barentsen ★ Space observatories have provided unprecedented depictions of the many variability behaviors

09 から 15：やや質量の大きい若い星の時間変動観測, 解析は緻密, 星と円盤がcorotationする半径の質量依存性を明らかにした.

26. **Tree-based solvers for adaptive mesh refinement code FLASH – II: radiation transport module TreeRay**
Richard Wünsch, Stefanie Walch, František Dinnbier, Daniel Seifried, Sebastian Haid, Andre Klepitko, Anthony P. Whitworth, Jan Palouš ★ The treatment of radiative transfer with multiple radiation sources is a critical challenge in

16 から 19：現実的なシュミレーションのために輻射場の取り扱い法を研究：輻射の源が複数の場合かつ広いエネルギー域の計算を可能にした.

27. **No impact of core-scale magnetic field, turbulence, or velocity gradient on sizes of protostellar disks in Orion A**
Hsi-Wei Yen, Bo Zhao, Patrick M. Koch, Aashish Gupta ★ We compared the sizes and fluxes of a sample of protostellar

05 から 08：研究目標はこの分野の最重要課題. 物理的因果関係がないから無相関だったのかもしれないが, 解析の粗さが目立つ, それに起因?

28. **TIMES I: a Systematic Observation in Multiple Molecular Lines Toward the Orion A and Ophiuchus Clouds**
Hyeong-Sik Yun, Jeong-Eun Lee, Yunhee Choi, Neal J. Evans II, Stella S. R. Offner, Mark H. Heyer, Brandt A. L. Gaches, Yong-Hee Lee, Giseon Baek, Minho Choi, Hyunwoo Kang, Seokho Lee, Ken'ichi Tatematsu, Yao-Lun Yang, How-Huan Chen, Youngung Lee, Jae Hoon Jung, Changhoon Lee, Jungyeon Cho ★ We have

01 から 04：オリオン南部を含めたおそらく始めての多輝線観測. 基本的なデータの提示論文.
だが堅実な解析, 続編を大いに期待.

26. **Tree-based solvers for adaptive mesh refinement code FLASH – II: radiation transport module TreeRay**

Richard Wünsch, Stefanie Walch, František Dinnbier, Daniel Seifried, Sebastian Haid, Andre Klepitko, Anthony P. Whitworth, Jan Palouš ★ The treatment of radiative transfer with multiple radiation sources is a critical challenge in

ABSTRACT

The treatment of radiative transfer with multiple radiation sources is a critical challenge in simulations of star formation and the interstellar medium. In this paper we present the novel TreeRay method for solving general radiative transfer problems, based on reverse ray tracing combined with tree-based accelerated integration. We implement TreeRay in the adaptive mesh refinement code FLASH, as a module of the tree solver developed by Wünsch et al. However, the method itself is independent of the host code and can be implemented in any grid based or particle based hydrodynamics code. A key advantage of TreeRay is that its computational cost is independent of the number of sources, making it suitable for simulations with many point sources (e.g. massive star clusters) as well as simulations where diffuse emission is important. A very efficient communication and tree-walk strategy enables TreeRay to achieve almost ideal parallel scalings. TreeRay can easily be extended with sub-modules to treat radiative transfer at different wavelengths and to implement related physical processes. Here, we focus on ionising radiation and use the On-the-Spot approximation to test the method and its parameters. The ability to set the tree solver time step independently enables the speedy calculation of radiative transfer in a multi-phase interstellar medium, where the hydrodynamic time step is typically limited by the sound speed of the hot gas produced in stellar wind bubbles or supernova remnants. We show that complicated simulations of star clusters with feedback from multiple massive stars become feasible with TreeRay.

Key words: galaxies: ISM – gravitation – hydrodynamics – ISM: evolution – radiative transfer

本研究の狙い

2017; Peters et al. 2017). Therefore, an efficient treatment of radiation transport in different energy bands (from the submillimeter to X-rays), and of the associated heating and cooling processes, is essential to simulate the structure and evolution of the ISM in detail, and to compare theoretical and numerical models with observations.

bient background radiation field. Hence, a modern radiative transfer algorithm must be able to handle multiple energy bands and multiple sources in an efficient manner.

2 THE ALGORITHM

3 ACCURACY AND PERFORMANCE TESTS

3.1 Spitzer test

SPITZER BUBBLE. The Spitzer bubble is one of the simplest models

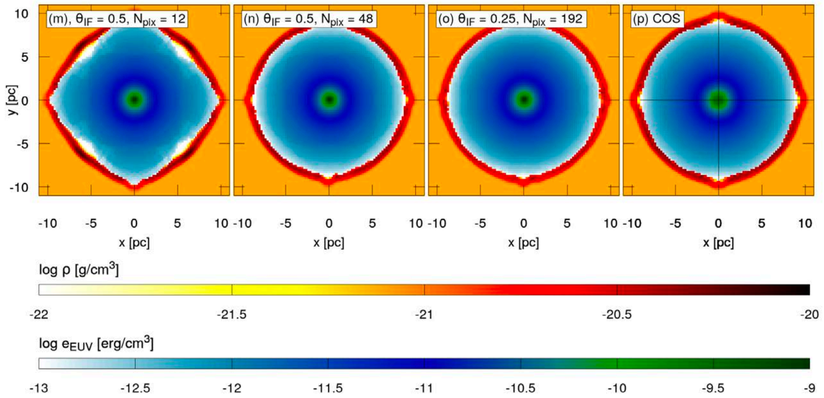

Figure 5. Spitzer test: the distribution of the radiation energy (blue-green) and the gas density (yellow-red), in the plane $z = 0$, at time 1.5 Myr, for models (a) through (p), as noted in the top left corner of each panel; see Table 1 for the model parameters. The logarithm of the radiation energy is shown in the region with non-zero ionisation degree, the logarithm of the gas density is shown in the remaining parts (i.e. for the neutral gas only).

3.3 Radiation driven implosion (RDI)

RDI. In this test we study a compact, dense, neutral cloud illuminated by ionising radiation from a single direction. The astronomical motivation is the cometary globules, commonly observed in Galactic HII regions, with bright rims on the side irradiated by a nearby hot star star (or stars) and tails pointing in the opposite direction (see e.g. Lefloch & Lazareff 1995; Deharveng et al. 2010;

3.4 Cloud irradiated by two sources

TWO-SOURCE MOTIVATION. This test assesses the fidelity of the code when treating a cloud that is irradiated by two identical sources, from different directions. Similarly to the previous tests (Sections 3.2.1

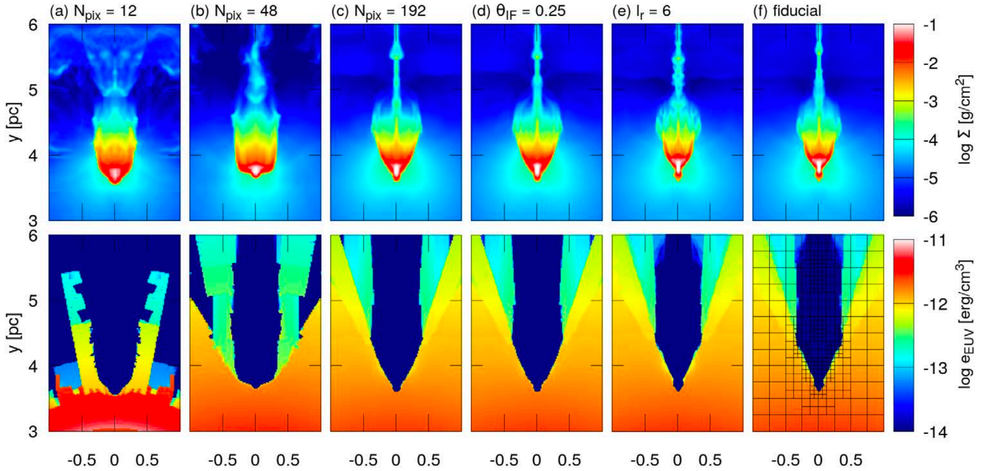

Figure 10. Radiation driven implosion test, comparison of models (a) through (f). The top panels show the logarithm of the gas column density. The bottom panels show the logarithm of the radiation energy density on the mid-plane. All models are plotted at time 180 kyr.

4 STAR FORMATION AND FEEDBACK WITH TREERAY

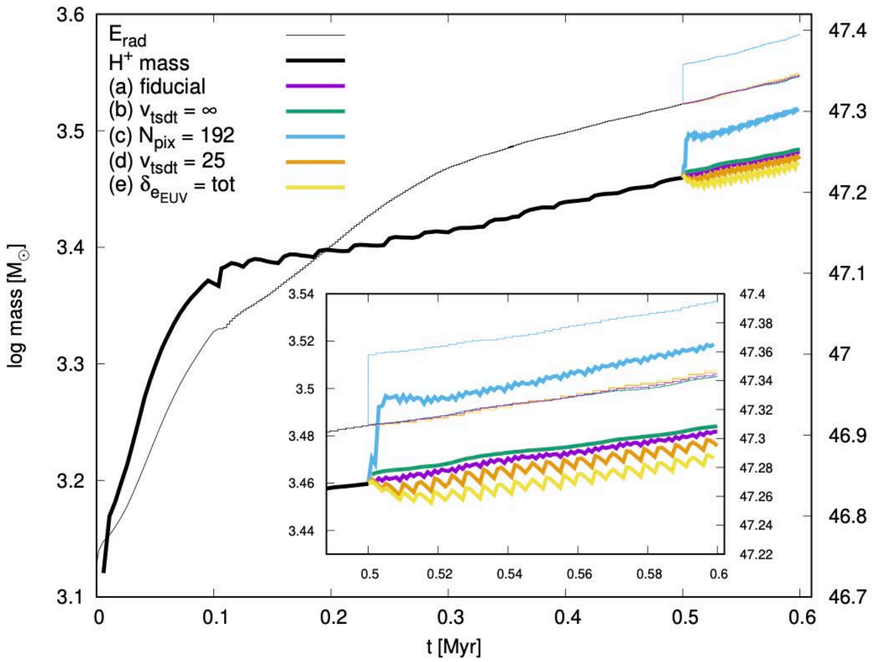

Figure 15. Star formation and feedback: the evolution of the total radiation energy, $E_{\rm rad}$, (thin lines, righthand ordinate), and the mass of ionised gas, $M_{\rm H^+}$, (thick lines, lefthand ordinate), in the whole computational domain, for models (a) through (e). The main figure shows the first 500 kyr of evolution for model (a) only (black lines). The inset shows the evolution between 500 and 600 kyr for all models. Note that, even at the resolution of the inset, the differences in $E_{\rm rad}$ between models (a), (b), (d) and (e) cannot be resolved.

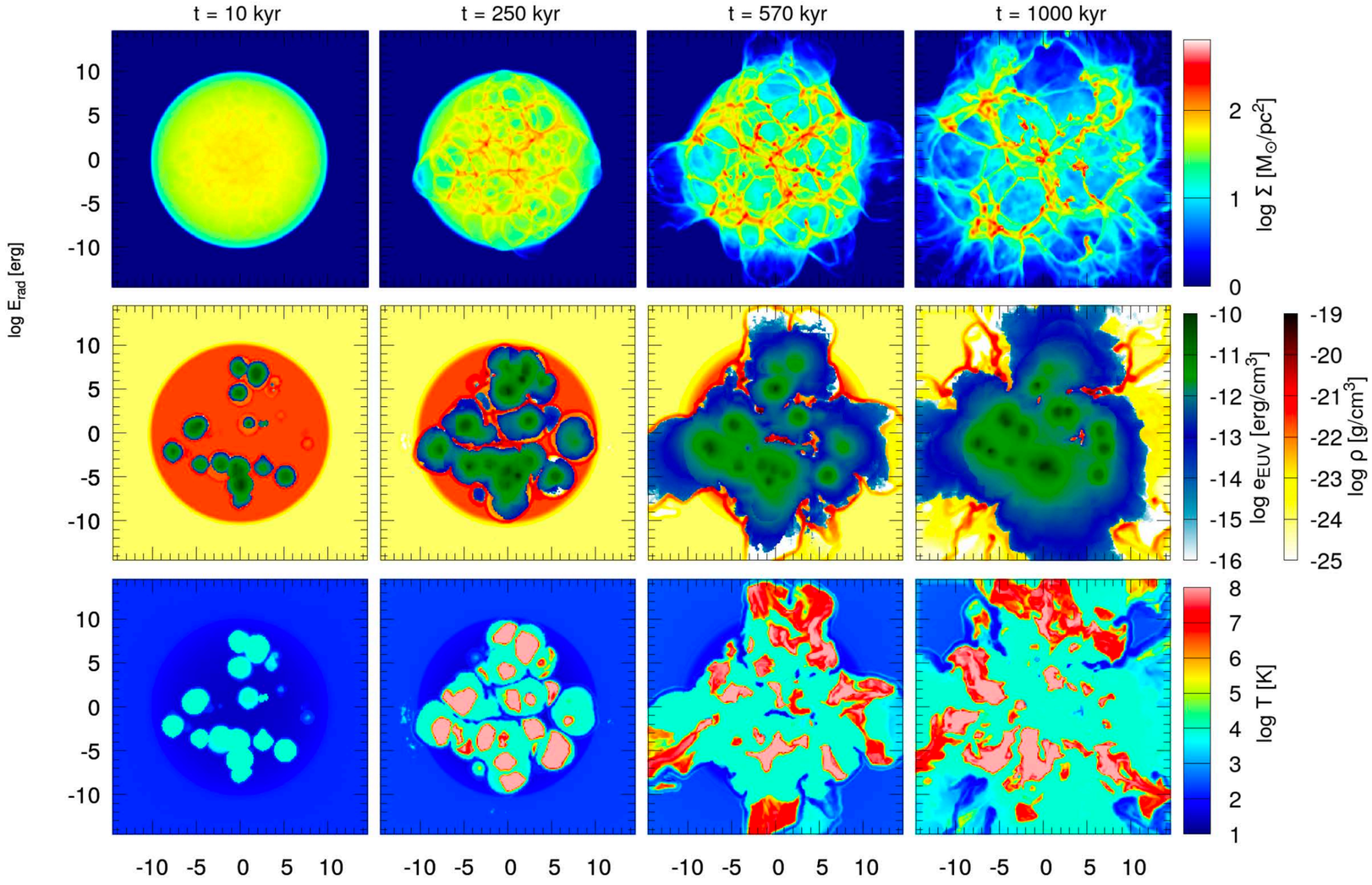

Figure 14. Star formation and feedback test: the fiducial model (a) at times $t = 10$, 250, 570 and 1000 kyr (from left to right). The top row shows the logarithm of the column density. The middle row shows the logarithm of the radiation energy, in the region with non-zero ionisation degree, and the logarithm of the gas density, in the remaining parts (i.e. for the neutral gas only). The bottom row shows the logarithm of the gas temperature. Panels in the middle and bottom rows show the quantities on the $z = 0$ plane.

SFN Letters速報ゼミ

July 15, 2021

古屋 玲

#342 24-28担当

24. **Thermal Wave Instability as an Origin of Gap and Ring Structures in Protoplanetary Disks**
Takahiro Ueda, Mario Flock, Tilman Birnstiel ★ Recent millimeter and infrared observations have shown that gap and

20

25. **Multicolor Variability of Young Stars in the Lagoon Nebula: Driving Causes and Intrinsic Timescales**
Laura Venuti, Ann Marie Cody, Luisa M. Rebull, Giacomo Beccari, Mike Irwin, Sowmya Thanvantri, Steve B. Howell, Geert Barentsen ★ Space observatories have provided unprecedented depictions of the many variability behaviors

09 から 15：やや質量の大きい若い星の時間変動観測, 解析は緻密, 星と円盤がcorotationする半径の質量依存性を明らかにした.

26. **Tree-based solvers for adaptive mesh refinement code FLASH – II: radiation transport module TreeRay**
Richard Wünsch, Stefanie Walch, František Dinnbier, Daniel Seifried, Sebastian Haid, Andre Klepitko, Anthony P. Whitworth, Jan Palouš ★ The treatment of radiative transfer with multiple radiation sources is a critical challenge in

16 から 19：現実的なシュミレーションのために輻射場の取り扱い法を研究：輻射の源が複数の場合かつ広いエネルギー域の計算を可能にした.

27. **No impact of core-scale magnetic field, turbulence, or velocity gradient on sizes of protostellar disks in Orion A**
Hsi-Wei Yen, Bo Zhao, Patrick M. Koch, Aashish Gupta ★ We compared the sizes and fluxes of a sample of protostellar

05 から 08：研究目標はこの分野の最重要課題. 物理的因果関係がないから無相関だったのかもしれないが, 解析の粗さが目立つ, それに起因?

28. **TIMES I: a Systematic Observation in Multiple Molecular Lines Toward the Orion A and Ophiuchus Clouds**
Hyeong-Sik Yun, Jeong-Eun Lee, Yunhee Choi, Neal J. Evans II, Stella S. R. Offner, Mark H. Heyer, Brandt A. L. Gaches, Yong-Hee Lee, Giseon Baek, Minho Choi, Hyunwoo Kang, Seokho Lee, Ken'ichi Tatematsu, Yao-Lun Yang, How-Huan Chen, Youngung Lee, Jae Hoon Jung, Changhoon Lee, Jungyeon Cho ★ We have

01 から 04：オリオン南部を含めたおそらく始めての多輝線観測. 基本的なデータの提示論文.
だが堅実な解析, 続編を大いに期待.

24. Thermal Wave Instability as an Origin of Gap and Ring Structures in Protoplanetary Disks

Takahiro Ueda, Mario Flock, Tilman Birnstiel ★ Recent millimeter and infrared observations have shown that gap and

Submitted to ApJL

ABSTRACT

Recent millimeter and infrared observations have shown that gap and ring-like structures are common in both dust thermal emission and scattered-light of protoplanetary disks. We investigate the impact of the so-called Thermal Wave Instability (TWI) on the millimeter and infrared scattered-light images of disks. We perform 1+1D simulations of the TWI and confirm that the TWI operates when the disk is optically thick enough for stellar light, i.e., small-grain-to-gas mass ratio of $\gtrsim 0.0001$. The mid-plane temperature varies as the waves propagate and hence gap and ring structures can be seen in both millimeter and infrared emission. The millimeter substructures can be observed even if the disk is fully optically thick since it is induced by the temperature variation, while density-induced substructures would disappear in the optically thick regime. The fractional separation between TWI-induced ring and gap is $\Delta r/r \sim 0.2$–0.4 at ~ 10–50 au, which is comparable to those found by ALMA. Due to the temperature variation, snow lines of volatile species move radially and multiple snow lines are observed even for a single species. The wave propagation velocity is as fast as ~ 0.6 au yr^{-1}, which can be potentially detected with a multi-epoch observation with a time separation of a few years.

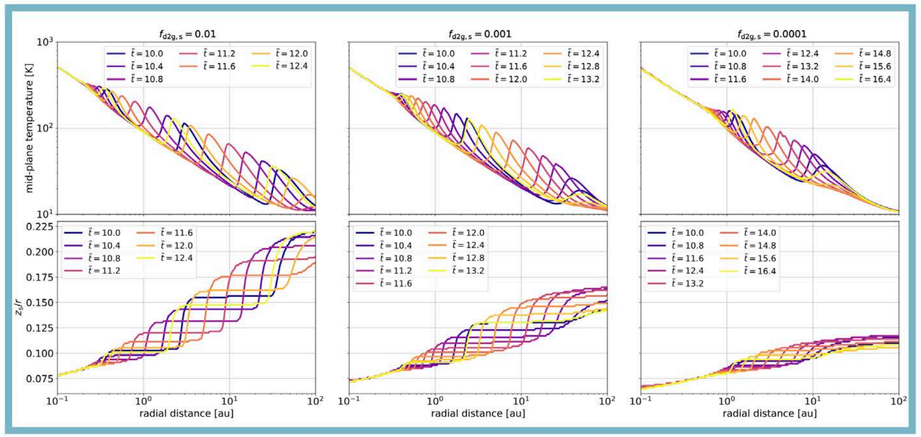

Figure 2. Time evolution of the mid-plane temperature (top) and the height of disk surface (bottom) for the model with $f_{d2g,s} = 0.01$ (left), 0.001 (center) and 0.0001 (right). An animated version of this figure provides the whole time evolution of the TWI from $\tilde{t} = 0$ to 19.8.

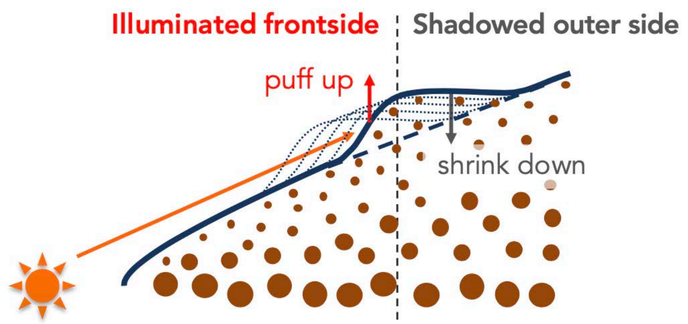

Figure 1. Schematic view of the thermal wave instability. The frontside of the perturbed disk surface receives more stellar flux and puffs up, while the shadowed outer side shrinks down (solid line). The perturbation propagates inward as a thermal wave (dotted lines).

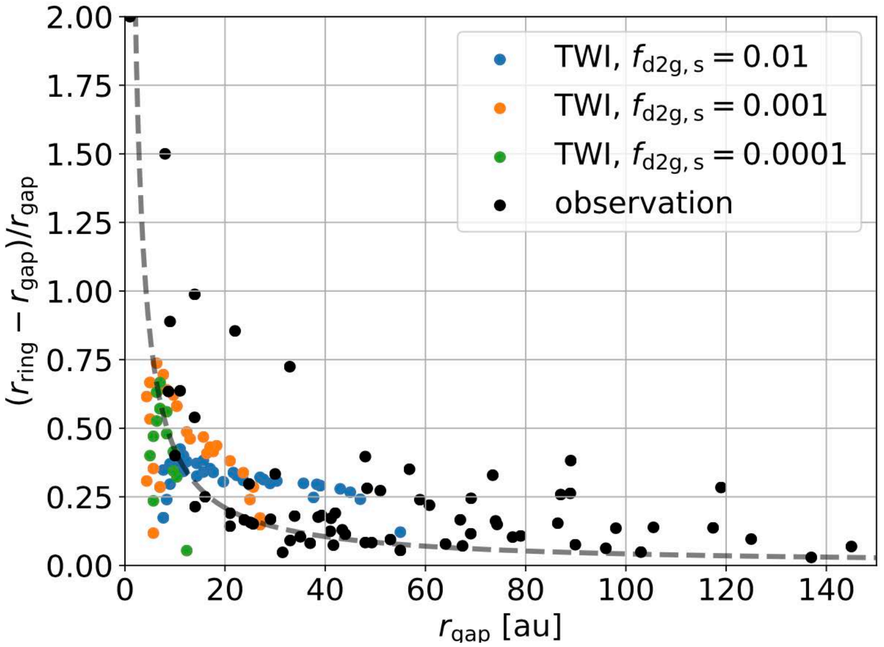

Figure 6. Fractional separation of observed and simulated gap and ring pairs. The observational data is compiled from Huang et al. (2018) and Long et al. (2018) (see also Andrews 2020). The gray dashed line denotes the condition for the ring-gap separation to be equivalent to the spatial resolution corresponding to an angular resolution of 0.″03 assuming the distance from the Earth of 140 pc, i.e., $\Delta r = 4.2$ au.